Chaotic Rabi vacuum oscillations in cavity quantum electrodynamics

L. E. Kon'kov and S. V. Prants[a)]
Pacific Oceanological Institute, Far-East Division of the Russian Academy of Sciences, 690041 Vladivostok, Russia

(Submitted 3 April 1997)
Pis'ma Zh. Éksp. Teor. Fiz. **65**, No. 11, 801–806 (10 June 1997)

It is shown in numerical simulations with two-level atoms moving through a single-mode high-Q cavity that spontaneous emission of a new type — chaotic Rabi vacuum oscillations — arises in the strong atom–field coupling regime. © *1997 American Institute of Physics.* [S0021-3640(97)00111-4]

PACS numbers: 12.20.Ds, 42.65.Sf, 32.20.Bv

In 1946 Purcell[1] called attention to the fact that the spontaneous emission rate of a two-level quantum system placed inside a cavity tuned to the quantum transition frequency ω_c is higher than in free space by a factor of $6Qc^3\pi/V\omega_c^3$. If the Q of the cavity $Q=\omega_c/\Delta\omega_c$, $\Omega_0/\Delta\omega_c>1$, is high enough, then the spontaneous emission becomes reversible, i.e., the system exchanges excitation with the field it has created at a rate Ω_0 equal to the Rabi vacuum frequency. Rabi vacuum oscillations have been observed both at Rydberg transitions of atoms in microwave cavities[2] and on optical transitions in microcavities.[3] This effect is a manifestation of one of the most fundamental interactions in nature — the dynamic interaction of matter with the vacuum. The ability to control spontaneous emission (its rate, spectral composition, and spatial structure) opens up wide prospects in technology for fabricating new high-efficiency radiators in microelectronics which employ microcavities and photonic band-gap materials.[4]

This letter will show by means of numerical simulations that under certain conditions a completely new type of spontaneous emission of atoms arises in small high-Q cavities — chaotic Rabi vacuum oscillations. We emphasize that the numerically discovered chaos in the interaction of excited atoms with the vacuum is dynamical (determinate), i.e., it arises as a result of an exponential instability of a purely dynamical atom–field system in a cavity that supports only one mode of the electromagnetic field and it is not a consequence of the absolute chaos of the physical vacuum itself. In principle, chaotic Rabi vacuum oscillations can arise in any region of the spectrum, but from the practical standpoint experiments with Rydberg atoms in microwave cavities and with ordinary atoms in optical microcavities are most promising.

In modern micromaser experiments Rydberg atoms prepared in a quantum state with a high principal quantum number are injected into a high-Q ($Q\simeq10^{10}$) single-mode microwave cavity ($\omega_f\simeq10^{11}$ rad/s) whose temperature is very low ($T\leqslant1$ K). Under such conditions the photon lifetime in the cavity, $T_f\simeq10^{-1}$–10^{-2} s, and the lifetime of the circulatory Rydberg states, $T_a\simeq10^{-2}$ s, are several orders of magnitude longer than the

period of the Rabi vacuum oscillations $T_0=2\pi/\Omega_0<10^{-4}$ s, and the transit time of atoms through the cavity $T_{\rm int}<10^{-5}$ s. In the strong atom–field coupling regime, $T_{\rm int}$, $T_0\ll T_a$, T_f, the atoms have enough time before leaving the cavity to exchange excitation many times with the field which they themselves have created. In this limit the dynamics of the atomic–field system is essentially Hamiltonian and can be described by a nonrelativistic Hamiltonian in the rotating-wave approximation:

$$H=\hbar\omega_a R_0+\hbar\omega_f(a^\dagger a+1/2)+\hbar\Omega_0(x)(a^\dagger R_-+aR_+). \tag{1}$$

The collective atomic operators

$$R_0=\frac{1}{2}\sum_{j=1}^{N}\sigma_z^j, \quad R_\pm=\sum_{j=1}^{N}\sigma_\pm^j \tag{2}$$

satisfy the commutation relations

$$[R_0,R_\pm]=\pm R_\pm, \quad [R_+,R_-]=2R_0. \tag{3}$$

The strength of the interaction of an atomic dipole with the vacuum field in the cavity is characterized by a Rabi vacuum frequency whose value depends on the location x of the atom:

$$\Omega_0(x)=|dE(x)|/\hbar. \tag{4}$$

Here d is the matrix element of the transition dipole moment between the working Rydberg levels, and

$$E(x)=\sqrt{\frac{2\pi\hbar\omega_f}{V}}f(x) \tag{5}$$

is the vacuum electric field at the point x. The function $f(x)$ characterizes the spatial structure of the selected mode on the x axis, along which the atoms move; it satisfies boundary conditions at the cavity walls; it is normalized to 1 at the maxima of the field; and, in the simplest case it has the form

$$f(x)=\sin kx=\sin\frac{2\pi gt}{L}, \tag{6}$$

where L is the size of the cavity along the x axis and g is the constant velocity of the atoms. In the microwave range the recoil energy of the atoms accompanying photon emission is very small $R=(\hbar\omega_f)^2/2mc^2\simeq 10^{-18}$ eV, so that the change in kinetic energy of the atoms can be neglected and only the evolution of their ''interior'' states need be studied (the Raman–Nath approximation). It is assumed that the size of an atomic bunch consisting of N atoms is much smaller than the wavelength of the microwave radiation ($\simeq 1$ cm). Therefore it can be assumed that $\Omega_0(x)$ is the same for all atoms.

The dynamics of the atom–field system is described by the Heisenberg equations for the atomic and field operators, which are ordinarily averaged over some quantum state, with all correlation functions of second and higher order factorized into a product of first-order correlation functions (semiclassical approximation). For atoms at rest, chaos is possible in the semiclassical approximation only if one abandons the rotating-wave approximation.[5] In a recent work[6] it was shown that semiclassical dynamical chaos arises

in a beam of moving atoms even in the rotating-wave approximation. However, in any case, the procedure of decoupling *all* quantum correlation functions results in a loss of spontaneous-emission sources. As a result, oscillations from an initial state with excited atoms and the vacuum field do not arise at all in the corresponding models. Spontaneous emission can be included in the theory by taking account of quantum correlations in the atomic subsystem in the decoupling procedure.[7]

We obtain the desired system of equations for the average values, taking account of the interatomic quantum correlations, from the Heisenberg equations for the operators $a^{\dagger}a$, $R_{+}R_{-}$, R_0, $aR_{+}+a^{\dagger}R_{-}$, and $i(a^{\dagger}R_{-}-aR_{+})$:

$$\dot{n}=-2\Omega\sqrt{N}fv, \quad \dot{v}=-(\omega-1)u-2\Omega f(1+2r+z+2Nnz)N^{-1/2},$$

$$\dot{u}=(w-1)v, \quad \dot{z}=4\Omega\sqrt{N}fv, \quad \dot{r}=-2\Omega N\sqrt{N}fzv, \quad \ddot{f}=-(b\omega)^2 f, \tag{7}$$

where a dot denotes differentiation with respect to the dimensionless time $\tau=\omega_a t$, and the variables are defined as follows:

$$n=N^{-1}\langle a^{\dagger}a\rangle, \quad u=N^{-3/2}\langle aR_{+}+a^{\dagger}R_{-}\rangle, \quad r=N^{-1}\left\langle \sum_{i\neq j=1}^{N}\sigma_{+}^{i}\sigma_{-}^{j}\right\rangle,$$

$$z=2N^{-1}\langle R_0\rangle, \quad v=iN^{-3/2}\langle a^{\dagger}R_{-}-aR_{+}\rangle. \tag{8}$$

The equation for the mode function f is included in the system of equations (7) so as to make the system autonomous.

Our model contains four dimensionless control parameters: the collective Rabi vacuum frequency $\Omega\equiv\Omega_0/2\omega_a$, the frequency detuning $\omega\equiv\omega_f/\omega_a$, the ratio $b\equiv g/c$ of the velocity of the atoms to the speed of light in free space, and the number N of atoms in the beam. The dynamical system obtained is nonlinear, and its solution subject to the initial condition

$$n(0)=u(0)=v(0)=r(0)=0, \quad z(0)=1, \tag{9}$$

describes Rabi vacuum oscillations. Besides a trivial integral of motion related with the mode function f, it also possesses two conservation laws

$$Nz^2+4r=C_1, \quad z+2n=C_2. \tag{10}$$

In the case of exact resonance, $\omega=1$, an additional integral of motion $u=$ const, characterizing the rate of energy exchange between the atomic and field subsystems, follows from the third equation of the system (7). It is the breakdown of this conservation law for

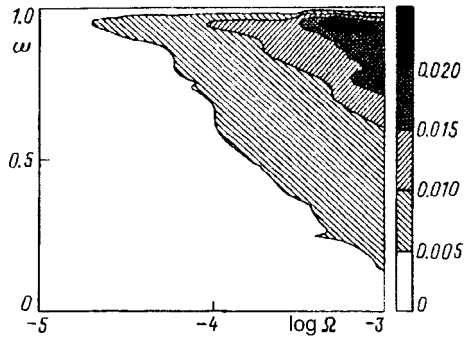

FIG. 1. Topographic λ map of the atom–field system in the ω–log Ω plane for $N=10^6$, $b=0.01$.

$\omega \neq 1$ that makes the system (7) nonintegrable. We note that for atoms at rest a similar conservation law also holds off-resonance. This is a consequence of the rotating-wave approximation.[8]

Numerical analysis of the dynamical atom–field system (7) showed that it is exponentially unstable off-resonance. As is well known, the exponential instability is characterized by a positive value of one of the Lyapunov exponents. We calculated the largest Lyapunov exponent λ in a wide range of values of the control parameters Ω, ω, b, and N. The so-called topographic λ maps, on which the values of λ are plotted in the plane as a function of the values of the two control parameters,[9] give a clear picture of the dynamical chaos.

A necessary condition for the onset and development of chaotic Rabi vacuum oscillations is that the characteristic times must conform to the following hierarchy:

$$T_R \ll T_{\rm cr} \leqslant T_{\rm int} \ll T_a,\ T_f, \tag{11}$$

where $T_R = 2\pi/\Omega_0\sqrt{N}$ is the period of the collective vacuum oscillations, $T_{\rm cr} = 1/\lambda\nu_a$ is the correlation decoupling time, and $T_{\rm int} = L/g$ is the transit time of the atoms through the cavity. We shall estimate the maximum value Ω_0 of the Rabi vacuum frequency $\Omega_0(x)$ for Rydberg atoms with a working transition frequency $\nu_a = 5\times 10^{10}$ Hz and dipole moment $d = 10^{-15}$ cgs units in a microcavity with volume $V = LR^2$, transverse size $R = 10^{-3}$ cm, and length $L = 1$ cm along the x axis, along which the atoms move. From Eqs. (4) and (5) we obtain $\Omega_0 \simeq 3\times 10^7$ rad/s. Numerical simulations show that for such values of the parameters, appreciable chaos with $\lambda = 6\times 10^{-3}$ will have set in for $N = 10^6$ atoms moving in a beam with velocity $v = 3\times 10^8$ cm/s ($b = 10^{-2}$). Estimates give $T_R \simeq 0.2$ ns, $T_{\rm int} \simeq 3.3$ ns, and $T_c \simeq 3.3$ ns. Therefore the conditions (11) hold.

Figure 1 shows a topographic λ map in the ω–log Ω plane for $N = 10^6$ and $b = 10^{-2}$. The map confirms that chaos is absent ($\lambda = 0$) at exact resonance ($\omega = 1$). The intensity of the chaos is characterized by the quantity λ, whose values are given on the scale on the right-hand side of the figure. The topographic λ map in the log b–log N plane gives a clear representation of the intensity of the chaos in different ranges of the values of the velocity and number of the atoms. In Fig. 2 it is shown for $\omega = 0.9$ and $\Omega = 10^{-3}$.

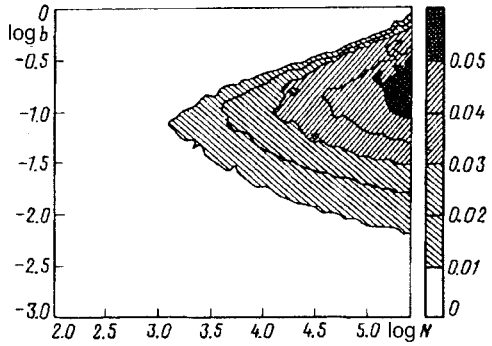

FIG. 2. Topographic λ map of the atom–field system in the log b–log N plane for $\omega=0.9$ and $\Omega=0.001$.

The largest Lyapunov exponent is an excellent diagnostic tool, but it cannot be measured directly in a real experiment. The dynamics of the number of photons $Nn(t)$ and of the atomic inversion $Nz(t)$ are difficult to observe in experiments with moving atoms. The physical quantity measured in such experiments is the intensity of the spontaneous emission from N atoms: $I(t)=I_0\langle R_+R_-\rangle$, where I_0 is the intensity of the spontaneous emission from one atom. Separating in the quantum correlation function $\langle R_+R_-\rangle$ the term responsible for the interatomic correlations, we obtain $I(t)=I_0N(r+z/2+1/2)$. The first term describes the collective spontaneous emission due to the correlation of individual atoms.[7] The sum of the second and third terms characterizes the contribution of the isotropic spontaneous emission. The combination of values of the control parameters ω, Ω, b, and N for which the spontaneous emission intensity $I(t)$ oscillates chaotically can be easily found from the λ maps (Figs. 1 and 2). As an illustration, Fig. 3 displays a typical spectrum of the intensity of this quantity on a logarithmic scale in the case of a chaotic process with $\lambda=0.05$ for $\omega=0.9$, $\Omega=10^{-3}$, $b=0.22$, and $N=10^5$. The computed power spectra (not shown here) for regular Rabi

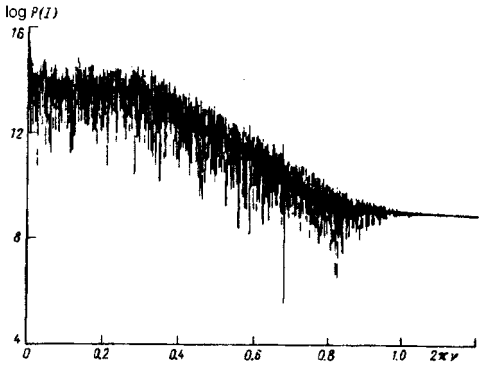

FIG. 3. Power spectrum of chaotic Rabi vacuum oscillations with a largest Lyapunov exponent $\lambda=0.05$ for $\omega=0.9$, $\Omega=10^{-3}$, $b=0.22$, and $N=10^5$.

vacuum oscillations ($\lambda \simeq 0$) have the characteristic structure of a quasiperiodic process with well-resolved individual peaks.

In conclusion, we underscore that our model of the atom–field dynamics (7), which takes account of the interatomic correlations, goes beyond the simple semiclasssical approximation[5,6,9] in which *all* correlations in the atom–field system are neglected. Nonetheless, dynamical chaos is found to be possible in the system even in the rotating-wave approximation. The numerical simulations performed and the estimates made show that in the case of atoms moving in the vacuum field of a high-Q microcavity and for physically reasonable values of the parameters the atom–field system undergoes a transition to a new type of spontaneous emission — chaotic Rabi vacuum oscillations.

The experimental realization of the regime of chaotic Rabi vacuum oscillations requires a high velocity of the atoms together with a small cavity volume (or a sufficiently high density of atoms). In the micromaser experiments known to us, the velocities of the atoms do not exceed 10^6 cm/s ($b \leqslant 10^{-5}$) and the transverse dimensions of the cavity do not exceed 1 mm.[2,4] For such values of b and R the largest Lyapunov exponent does not exceed the computational error in our calculations, i.e., the Rabi vacuum oscillations are substantially (quasi)periodic. To distinguish dynamical chaos against the background of random processes which are unavoidable in a real experiment, experiments with resonant atoms could be helpful. As our analytical and numerical results show, dynamical chaos is certainly impossible (at least in the rotating-wave approximation) in the case of exact resonance of the atoms with a selected cavity mode.

This work was supported by the Russian Fund for Fundamental Research under Projects Nos. 96-0-19827 and 96-02-18746.

[a)]e-mail: prants@medphys.marine.su

[1] E. M. Purcell, Phys. Rev. **69**, 681 (1946).
[2] Y. Kaluzny, P. Goy, M. Gross *et al.*, Phys. Rev. Lett. **51**, 1175 (1983).
[3] R. J. Tompson, G. Rempe, and H. J. Kimble, Phys. Rev. Lett. **68**, 1132 (1992).
[4] J. Rarity and C. Weisbuch (eds.), *Microcavities and Photonic Bandgaps: Physics and Applications*, Kluwer Academic Publishers, Dordrecht, 1996.
[5] P. I. Belobrov, G. M. Zaslavskiĭ, and G. Kh. Tartakovskiĭ, Zh. Éksp. Teor. Fiz. **71**, 1799 (1976) [Sov. Phys. JETP **44**, 945 (1976)].
[6] S. V. Prants and L. E. Kon'kov, Phys. Lett. A **225**, 33 (1997).
[7] A. V. Andreev, V. I. Emel'yanov, and Yu. A. Il'inskiĭ, *Cooperative Phenomena in Optics* [in Russian], Nauka, Moscow, 1988.
[8] E. T. Jaynes and F. W. Cummings, Proc. IEEE **51**, 89 (1963).
[9] S. V. Prants and L. E. Kon'kov, Izv. Ross. Akad. Nauk, Ser. Fiz. **60**, 178 (1996).

Translated by M. E. Alferieff

Boltzmann spectral distribution or ''infrared catastrophe'' in the resonance radiation of a gas

Yu. K. Zemtsov, A. Yu. Sechin, and A. N. Starostin
Troitsk Institute of Innovational and Thermonuclear Research, 142092 Troitsk, Moscow Region, Russia

A. G. Leonov and D. I. Chekhov
Moscow Physicotechnical Institute, 141700 Dolgoprudnyĭ, Moscow Region, Russia

(Submitted 4 April 1997; resubmitted 5 May 1997)
Pis'ma Zh. Éksp. Teor. Fiz. **65**, No. 11, 807–811 (10 June 1997)

The purely thermal infrared emission spectra of a resonance medium (sodium vapor) are investigated experimentally. It is shown that the emission intensity in the 2–3 μm range at temperatures of 600–1200 K is several orders of magnitude higher than the intensity obtained from the standard theory of resonance radiation transfer. This phenomenon can be conventionally termed an ''infrared catastrophe.'' The form of the recorded spectra and the absolute intensity of the emission in both the infrared and visible regions of the spectrum are in agreement with the theory developed by Yu. L. Zemtsov and A. M. Starostin, Zh. Éksp. Teor. Fiz. **103**, 345 (1993) [JETP **76**, 186 (1993)], in which the Boltzmann spectral distribution of the population of the resonance level is proportional to $\exp(-\hbar\omega/T)$. © *1997 American Institute of Physics.* [S0021-3640(97)00211-9]

PACS numbers: 52.25.Rv, 51.70+f

Important results in agreement with many experimental data have been obtained in the theory of resonance radiation transfer.[1,2] However, in some limiting cases this theory is in conflict with fundamental laws. This refers specifically to the narrow-line approximation ($\Delta\omega=\omega-\omega_0\ll\omega_0$, where ω_0 is the resonance transition frequency), in which the spectral intensity of the volume radiation of a resonance medium is described by the expression[1,2]

$$\epsilon_\omega=(1/4\pi)\hbar\omega_0 AN^*(\omega), \tag{1}$$

where A is the spontaneous emission probability, $\hbar$ is Planck's constant, and $N^*(\omega)$ is the spectral population density of the resonance level, i.e., the density of atoms capable of emitting photons with frequency ω (in the approximation of complete frequency redistribution of the absorbed and emitted photons it is assumed that $N^*(\omega)=N^*a(\omega)$, where N^* is the total population of the resonance level and $a(\omega)$ is the line profile). However, as shown in Ref. 3, assuming that at equilibrium $N^*=N_0\exp(-\hbar\omega_0/T)$ (Ref. 1; the degeneracies are assumed to be equal, T is the temperature, and N_0 is the population of the ground state), the correct expression for the equilibrium Planck intensity J_P cannot be obtained from Eq. (1), since that expression contains the resonance frequency ω_0, and

not the frequency variable ω. To obtain the correct formula for J_P, the expression for $N^*(\omega)$ must be modified by introducing into it a correction factor[2,3]

$$\tilde{N}^*(\omega)=N^*a(\omega)\exp(-\hbar(\omega-\omega_0)/T). \tag{2}$$

At equilibrium we shall have a Boltzmann spectral distribution

$$\tilde{N}^*(\omega)=N_0a(\omega)\exp(-\hbar\omega/T) \tag{3}$$

(in the absence of equilibrium $\tilde{N}(\omega)$ is found from the kinetic equations presented in Ref. 3). The total population of excited atoms is determined by the integral of expression (2) over the frequency and, for example, for purely radiational broadening it can be written in the form

$$\tilde{N}^*\simeq N_0\left\{\exp(-\hbar\omega_0/T)+\frac{3!}{2\pi}\frac{A}{\omega_0}\left[\frac{T}{\hbar\omega_0}\right]^4\right\}. \tag{4}$$

It is interesting that a similar sum of an exponential and a power-law contribution has also been obtained in the momentum distribution of the particles.[4]

Introducing the factor $\exp(-\hbar(\omega-\omega_0)/T)$ has virtually no effect on the shape of the line core $\Delta\omega\ll\omega_0$, but at temperatures $T\ll\omega_0$ it can give rise to a second maximum in the far ''red'' wing of the line profile in the region of several T (for a plasma this fact was noted in Ref. 3). In this case, a large fraction of the energy emitted in the line can lie in the nonresonance ''red'' wing and not in the near-resonance central part. We shall conventionally term this fact an ''infrared catastrophe.'' We also note that the absorption coefficient in this wing is small, and that ''soft'' photons can escape from a bounded medium.

Our objective in the present work was to observe experimentally a second maximum in the far ''red'' wing of a resonance line and to perform absolute measurements of the line intensity in the near-resonance and low-frequency parts of the line profile so as to check the theory developed in Refs. 3 and 5. The emission in such a far wing of a spectral line has not been studied previously (as a rule, the measurements have been confined to detunings $\leqslant$1000 cm^{-1}; see, for example, Ref. 6). Sodium vapor heated steadily to temperatures of 600–1200 K was used as the resonance medium. The emission in the 3P-3S resonance doublet was studied. For this doublet, at the temperatures indicated, the second maximum lies in the infrared (IR) region in the range 2–5 μm. We note especially that the purely thermal emission from the vapor in the absence of excitation of the vapor by an electric field or by an external radiation source was detected. Under these conditions the electron density is negligibly low, as are the intensities of the bremsstrahlung and photorecombination continuua. The relatively low temperatures also rule out the appearance of thermal radiation in other lines in this region of the spectrum.

The investigations were performed on an apparatus consisting of a cylindrical ''heat pipe'' type cell, filled with sodium vapor, and a recording system. Prior to the experiments, the cell containing metallic sodium was evacuated, filled with argon to a pressure of 1 atm, and heated to the required temperature. Two detectors, calibrated with respect to absolute sensitivity, directly recorded in the paraxial zone of the pipe the radiation entering through a window at the end of the pipe. The radiation in the visible part of the

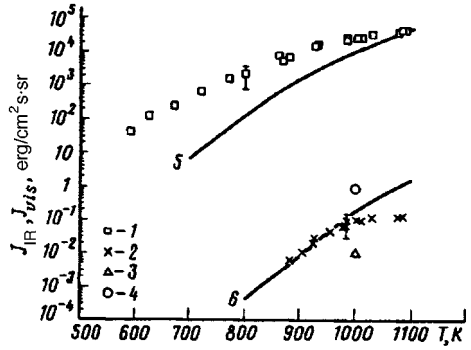

FIG. 1. Integrated emission intensities of sodium vapor in the IR (*1*, *3*, *5*) and visible (*2*, *4*, *6*) regions of the spectrum versus temperature at the center of the heat pipe: *1*, *2* — Experiment; *3*, *4* — standard theory; *5*, *6* — theory of Ref. 3.

spectrum (0.5–0.6 μm band, cut out by a collection of light filters) was recorded with a FÉU-84 photomultiplier, and the radiation in the IR region (2–3 μm band) was recorded with a photodetector based on a PbS photoresistor with a germanium window. To obtain the IR emission spectra (with resolution ~ 300 cm^{-1}) the radiation was directed onto the input slit of an IR monochromator and a pyroelectric detector was placed at the output of the same monochromator. Special care was taken in the experiments to prevent the direct radiation from the heated cell walls from entering the detector apertures. To this end, two diaphragms, which limited the solid angle of the radiation striking the detectors, were placed between the detectors and the cell. We note that when the diaphragms were installed with no sodium in the cell, even at the maximum temperatures the signal from the detectors was below the sensitivity level of the recording apparatus, irrespective of the presence and pressure of argon in the cell.

The experimentally obtained temperature dependence of the integrated (over the above-indicate wavelength ranges) intensity of the radiation emission from the vapors in the visible ($J_{\rm vis}$) and IR ($J_{\rm IR}$) regions of the spectrum is presented in Fig. 1 and their IR emission spectra for different temperatures T are displayed in Fig. 2. It follows from the data presented that the IR emission intensity is several orders of magnitude higher than the intensity in the near-resonance region of the spectrum, and a readily observable peak is observed in the IR part of the spectrum, qualitatively confirming the theory.

For quantitative comparison with the experimental data, numerical calculations taking account of the temperature distribution measured along the axis of the cell were performed on the basis of the theory of resonance radiation transfer developed in Refs. 3 and 5. The Na atom density distribution corresponding to saturated vapor pressure[7] was used (this is valid at least up to temperatures of the order of 800–900 K; Ref. 8). It was assumed in the calculations that the optically transparent ''red'' wing of the resonance line is formed by quasistatic broadening by argon.[9] The theory of Ref. 5, which takes account of the strong dispersion of a resonant gas at high density, was used for numerical modeling near the line center. Figure 3 displays the frequency dependences of the radiation intensity at the center of the cell for a fixed temperature $T=1000$ K. Curve *1*

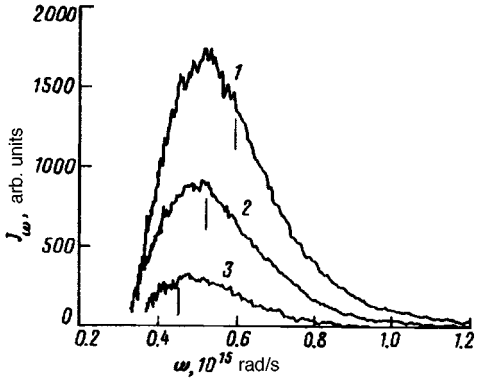

FIG. 2. Thermal emission spectrum of sodium vapor in the IR region of the spectrum for different temperatures at the center of the heat pipe: *1* — $T=1080$ K, *2* — 950 K, *3* — 830 K. The vertical bars show the positions of the peaks according to the theory of Ref. 3.

corresponds to the theory of Ref. 3, taking account of the exponential factor $\exp(-\hbar(\omega-\omega_0)/T)$; curve *2* corresponds to the standard theory of the radiation in a spectral line,[1] and curve *3* corresponds to the Planckian intensity. In the IR region of the spectrum the theory of Ref. 3 gives for the radiation intensity a value several orders of magnitude higher than that obtained in the standard theory. On the ''blue'' wing the situation is reversed and, especially importantly, the frequency integral of the intensity calculated by the standard theory diverges at high frequencies. We note that a narrow peak with a higher intensity than the Planckian peak is clearly seen at line center in the curve *1*. This peak is due to the strong dispersion and absorption in the dense sodium vapor, as discussed in detail in Refs. 5 and 10. Figure 4 shows the spectral curves of the thermal radiation emitted from the cell. In addition, the shape and position of the peak in

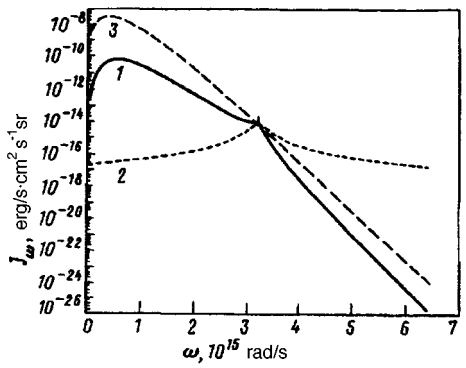

FIG. 3. Frequency dependences of the spectral radiation intensities at the center of the cell for $T=1000$ K: *1* — Calculation according to the theory of Ref. 3, *2* — calculation according to the standard radiation theory,[1] *3* — Planck intensity.

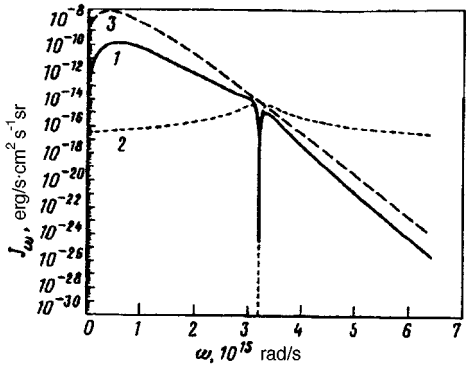

FIG. 4. Frequency dependence of the spectral intensities of the radiation leaving the cell ($T=1000$ K): *1* — Calculation according to the theory of Ref. 3, *2* — calculation according to the standard radiation theory,[1] *3* — Planck intensity.

the observed spectral dependence of the emission intensity in the ''red'' wing are in agreement with the calculations (compare Figs. 2 and 4).

Figure 1 displays the calculations, performed according to the theory of Ref. 3, of the integral intensity of the radiation in the spectral regions corresponding to experiment. As follows from the plots, the theoretical curve for the region 0.5–0.6 μm is in good agreement with experiment. For the IR region, however, the experimental and computed data are in order-of-magnitude agreement with one another. The discrepancy can be explained on the one hand by the imperfection of the theory, which describes approximately the formation of a static wing at such large detunings, and on the other by the absence of accurate data on the distribution of the vapor density along the cell. The far wings of the molecular lines of Na_2 molecules can also contribute to the IR radiation of the vapor. However, the number of such molecules is small. We note that the contribution of the wings of resonance transitions in argon atoms is negligibly small because of their high excitation potential; this is confirmed by the fact that there are no emission signals in the absence of Na vapor.

The integrated intensities obtained from the standard theory differ impressively from the observed values (see Fig. 1), being several times higher in the visible region and almost six orders of magnitude lower in the IR part of the spectrum. Thus the experimental data are in complete agreement with the theory developed in Ref. 3, where the Boltzmann distribution of the spectral population of a resonance level is proportional to $\exp(-\hbar\omega/T)$, and they confirm the presence of an ''infrared catastrophe'' in the radiation emission from a resonant medium. It should be noted that, in reality, the exponent factor $\exp(-\hbar\omega/T)$ in the spectral distribution of the excited atoms arises (see Ref. 3) both as a result of collisional excitation processes and collisions of the second kind, if the radiation escaping from a bounded medium has only a weak effect on the equilibrium in the medium (which happens in our case, since $\Gamma \gg A$, where Γ is the collisional width), and on account of the external equilibrium radiation (which also happens under our conditions, since the radiation from the cell walls is nearly black-body radiation). Furthermore, we note that the same factor can also be obtained by studying the collisionally induced

emission.[11,12] However, the probability of this process is determined by the inelastic collision cross section of argon and sodium atoms, which is negligibly small because of adiabatic exclusion.

In closing, we note that as the temperature increases, the ratio of the integrated intensities in the visible and IR regions of the spectrum changes. As the calculations showed, for Na vapor $J_{vis} > J_{IR}$ at $T > 3500$ K. Nonetheless, even at high temperatures the contribution of the ''red'' wings of the resonance line continues to remain much higher than that computed in the standard theory. This could be important in calculations and measurements of radiation emission from plasma and light sources and in the interpretation of measurements performed in the solar spectrum, since the emission intensity in the far ''red'' wings can compete with the intensity determined by other emission mechanisms (bremsstrahlung and so on).

We are deeply grateful to Academician A. M. Dykhne (RAN), P. D. Gasparyan, Yu. K. Kochubeĭ, and A. A. Panteleev for their interest in this work and for stimulating discussions and Corresponding Member V. D. Shafranov (RAN) and the participants of his seminar for fruitful discussions. We are also grateful to A. A. Rudenko for substantial assistance in the experiments. This work was supported by the Russian Fund for Fundamental Research under Grants Nos. 96-02-17390 and 97-02-17796 and the International Scientific and Technical Center under Project No. 076/95.

[1] L. M. Biberman, V. S. Vorob'ev, and I. T. Yakubov, *Kinetics of Nonequilibrium Low-Temperature Plasmas*, Plenum Press, New York, 1987 [Russian original, Nauka, Moscow, 1982].
[2] D. Mihalas, *Stellar Atmospheres*, W. H. Freeman, San Francisco, 1978 [Russian translation, Mir, Moscow, 1982].
[3] Yu. L. Zemtsov and A. N. Starostin, Zh. Éksp. Teor. Fiz. **103,** 345 (1993) [JETP **76**, 186 (1993)].
[4] V. M. Galitskiĭ and V. V. Yakimets, Zh. Éksp. Teor. Fiz. **51,** 957 (1966) [Sov. Phys. JETP **24**, 637 (1967)].
[5] Yu. K. Zemtsov, A. Yu. Sechin, and A. N. Starostin, Zh. Éksp. Teor. Fiz. **110,** 1654 (1996) [JETP **83**, 909 (1996)].
[6] M. J. Jongerius, in *Spectral Line Shapes*, edited by B. Wende, Berlin, 1980.
[7] *Physical Quantities* [in Russian], Énergoatomizdat, Moscow, 1986.
[8] D. I. Chekhov, *Candidate's Dissertation* [in Russian], Moscow Physicotechnical Institute, Moscow, 1994.
[9] I. E. Sobel'man, *Introduction to the Theory of Atomic Spectra*, Pergamon Press, New York, 1972 [Russian original, Fizmatgiz, Moscow, 1966].
[10] Yu. K. Zemtsov, A. Yu. Sechin, A. N. Starostin *et al.*, JETP Lett. **65**, 13 (1997).
[11] V. A. Kas'yanov and A. N. Starostin, Zh. Éksp. Teor. Fiz. **48**, 295 (1965) [Sov. Phys. JETP **21**, 193 (1965)].
[12] J. Borisov and L. Frommhold, in *Phenomena Induced by Intermolecular Interaction*, edited by G. Birnbaum, Plenum Press, New York, 1985.

Translated by M. E. Alferieff

Theory of average pulse propagation in high-bit-rate optical transmission systems with strong dispersion management

S. K. Turitsyn[a)]
Institute of Automation and Electrometry, 630090 Novosibirsk, Russia

(Submitted 8 May 1997)
Pis'ma Zh. Éksp. Teor. Fiz. **65**, No. 11, 812–817 (10 June 1997)

A theory of signal transmission in high-bit-rate optical communication systems with large variations of dispersion (strong dispersion management) is presented. It is found that the averaged propagation of a chirped breathing optical pulse along the line is described by the nonlinear Schrödinger equation with an additional parabolic potential. The shape of the averaged pulse is intermediate between the sech-type soliton and a Gaussian pulse. The rapidly decaying Gaussian wings of such pulses allow denser information packing in comparison with the use of sech-type fundamental solitons. © *1997 American Institute of Physics.* [S0021-3640(97)00311-3]

PACS numbers: 42.65.−k

Ultrafast optical signal transmission is an example of the successful practical utilization of the fundamental results of modern soliton theory. Impressive results have been achieved recently in long-distance, high-bit-rate optical data transmission by using an optical soliton (a pulse resulting from a balance between fiber nonlinearity and dispersion) as the information carrier. The stable, error-free, multichannel (10 Gbit/s per channel) soliton transmission has been demonstrated over transoceanic distances.[1] The theory of signal transmission in optical fiber lines is based on the nonlinear Schrödinger equation (NLSE) which was integrated by Zakharov and Shabat in 1971.[2] The NLSE is one of the fundamental nonlinear models integrable by means of the powerful inverse scattering transform method. The properties of the sech-profile soliton solution of the NLSE determine the features of the optical communication lines utilizing the soliton concept.

One of the main factors limiting transmission capacity achievable by the modern optical soliton-based communication systems[3] is the interaction between two neighboring solitons. Overlap of the exponential tails of closely spaced pulses leads to interaction of the solitons and to information loss. To provide for stable transmission, the separation between two neighboring fundamental solitons should be not less than five soliton widths. This is a fundamental limitation for a transmission based on the sech-shaped soliton described by the NLSE.

One possible way of increasing the transmission capacity is to use as the information carrier a solitary wave with wings decaying faster than exponential tails of the NLSE soliton. This would result in a substantial suppression of the soliton interaction and thus in the possibility of denser information packing. This letter presents a theory of nonlinear

communication systems that permit the stable transmission of a soliton with rapidly decaying tails. Specifically, we describe the propagation of a soliton with Gaussian wings in an optical transmission system with dispersion compensation.

The dispersion compensation technique recently been the focus of intensive research as a promising approach to increasing the transmission capacity of optical communication systems in both the linear and soliton regimes (see, e.g., Refs. 4–15 and references therein). In the linear regime, compensation of the dispersion prevents dispersive broadening of the pulse. An additional advantage is that the impact of four-wave mixing on the signal transmission is suppressed due to a reduction in the efficiency of the phase matching. In the soliton regime, numerical simulations and experiments demonstrate extremely stable propagation of a soliton in fiber links with dispersion compensation. Large variation of the dispersion leads to the breathing-like oscillations of the pulse width as a function of the amplification length; the ''slow'' dynamics on larger scales is governed by the fiber nonlinearity and the residual dispersion.[7] Numerical simulations reveal the following features of the breathing soliton:

— the form of the asymptotic pulse is closer to a Gaussian shape rather than to a sech-profile;

— the pulse that forms is chirped (the pulse phase has a nontrivial time dependence);

— the energy of the stable breathing pulse is well above that of the NLSE soliton with the corresponding average dispersion.

These observations make clear the difference between a soliton-like pulse in a system with dispersion compensation and the soliton of the NLSE. This indicates that an average model describing the evolution of the breathing pulse should differ from the NLSE.

In this letter a basic equation describing the slow dynamics of a chirped pulse in transmission systems with strong dispersion management is derived in leading order. It is found that the average propagation of the chirped pulse is described by the NLSE with an additional quadratic potential. It is demonstrated that a stationary pulse is an intermediate state between the NLSE sech-type soliton and a Gaussian pulse. The theory developed here for a soliton with Gaussian wings propagating in a transmission system with dispersion compensation explains the numerical and experimental observations mentioned above.

Optical pulse propagation down a cascaded transmission system with dispersion compensation is governed by the equation

$$iA_z + d(z)A_{tt} + |A|^2 A = iZ_{NL}\left(-\gamma + [\exp(\gamma Z_a) - 1]\sum_{k=1}^{N} \delta(z - z_k) \right) A = iG(z)A. \quad (1)$$

We use here the notation of Ref. 7: $Z_{NL} = 1/\sigma P_0$ is the nonlinear length, $Z_{\mathrm{dis}} = t_0^2/|\beta_2|$ is the dispersion length corresponding to the transmission fiber (standard monomode fiber (SMF)); t_0 and P_0 are the incident pulse width and peak power, β_2 is the group velocity dispersion for a SMF; σ is the coefficient of the nonlinearity, and γ describes the fiber losses. The retarded time is measured in units of the initial pulse width, $t = T/t_0$; the

envelope of the electric field $E=E(T,Z)$ is normalized to the initial pulse power, $|E|^2=P_0|A|^2$; and the coordinate along the fiber z is in units of the nonlinear length, $z=Z/Z_{NL}$, where Z_a is amplification period, and $z_k=kz_a$ are the locations of the amplifiers. The chromatic dispersion $d(z)=\tilde{d}(z)+\langle d\rangle$ is the sum of a rapidly varying part ($\tilde{d}\sim Z_{NL}/Z_{\rm dis}\gg 1$) and a constant residual dispersion ($\langle d\rangle\sim Z_{NL}/Z_{RD}\sim 1$), where $Z_{RD}=t_0^2/|\beta_{2RD}|$ is the dispersion length corresponding to the residual dispersion of each section. The simplest optical-pulse equalizing system consists of a transmission fiber and equalizer fiber with the opposite dispersion — a dispersion-compensating fiber. Incorporation of a fiber with normal dispersion reduces (or in the ideal case eliminates) the total dispersion of the fiber span between two amplifiers. The term ''strong dispersion management'' means that the variation of the dispersion over the amplification period is large. Consequently, not only the pulse power but also the pulse width undergoes substantial variation during the amplification period. Formally this can be stated as the condition $R(z)=\int_0^z d(z')dz'\geqslant 1$.

As we have said, an optical pulse propagating in a system with a large variation of the dispersion experiences periodic oscillations of the amplitude and width. The rapid breathing oscillations of the pulse are accompanied by slow average changes of the pulse characteristics due to nonlinearity and residual dispersion.[7] In the limit Z_a, $Z_{\rm dis}\ll Z_{NL}$, Z_{RD}, one may treat the nonlinearity and residual dispersion as perturbations. Therefore, let us first recall the well-known exact solution of the linear problem. If we neglect the nonlinear term in Eq. (1), the fast oscillations of the linear pulse amplitude and width for a Gaussian input signal $A(0,t)=N\exp(-t^2)$ are given by

$$A(z,t)=\frac{N}{\sqrt{\tau(z)}}\exp(-t^2/\tau^2(z)-iCt^2/\tau^2(z)+i\Phi(z))\exp\left(\int_0^z G(z')dz'\right), \qquad (2)$$

where $\tau^2(z)=1+16R^2(z)$, $dR(z)/dz=d(z)$, $C=4R(z)$ and $\Phi=-0.5\tan^{-1}[4R(z)]$. This solution shows that the pulse is highly chirped, in contrast to the soliton solution of the NLSE. We demonstrate later that this chirping leads to an effective parabolic potential in the equation describing the slow dynamics. Nonlinear effects come into play on a scale large compared to Z_a, namely over distances proportional to Z_{NL}. The nonlinear length Z_{NL} can be comparable with Z_{RD}. Therefore, in the description of the average evolution of the pulse, it is necessary to take into account both the residual dispersion and nonlinearity. Thus there are two scales in the pulse dynamics:[7] fast processes, corresponding to large oscillations of the amplitude and the width of the pulse, and slow dynamics, giving the average changes due to nonlinear effects and residual dispersion. The fast oscillations are only slightly modified by nonlinearity and residual dispersion. Note that the slow average dynamics is responsible for the stability of signal transmission. Our goal now is to average Eq. (1) keeping the general structure of the rapid oscillations given by (2).

The large variation of the dispersion over the amplification period is the main obstacle to the direct application of the powerful Lie-transform[16] method of obtaining the averaged (slow) dynamics in Eq. (1). The main technical idea of the approach suggested here is first to use a transformation that takes the fast pulse dynamics into account and then to apply an averaging procedure to the transformed equation. As we demonstrate,

this allows one to derive an averaged model that is the NLSE with an additional parabolic potential responsible for the formation of the Gaussian wings of the soliton. This procedure is a modification of the averaging procedure used in Ref. 7. The important difference is that in the approach developed here, the pulse chirp (phase dependence) is taken into account by an exact transform, and therefore a local (nonintegral) average equation is obtained. Since nonlinearity and residual dispersion act as small perturbations to the linear dynamics, we initially assume that the pulse dynamics will have a structure close to that given by Eq. (2).

Let us make the following transformation that is similar to the so-called ''lens'' transformation first suggested by Talanov in the theory of self-focusing:[17]

$$A(t,z)=\frac{Q(\xi,z)}{\sqrt{\tau(z)}}\exp\left[i\frac{\nu(z)}{\tau(z)}t^2\right]\exp\left(\int_0^z G(z')dz'\right), \tag{3}$$

where $\xi=t/\tau$ and

$$d\tau/dz=4d(z)\nu. \tag{4}$$

Equation (1) is transformed to

$$iQ_z+\frac{d(z)}{\tau^2}Q_{\xi\xi}+\frac{c(z)}{\tau}|Q|^2Q-\tau\nu_z\xi^2Q=0. \tag{5}$$

We still have freedom to choose the equation for ν_z. Let us fix the latter as

$$\nu_z=a^2\left[\frac{d(z)}{\tau^3}-\frac{c(z)}{\tau^2}\right];\quad c(z)=\exp\left(2\int_0^z G(z')dz'\right). \tag{6}$$

Note that although Eqs. (4), (6) were derived in Ref. 7 using a variational approach, here these equations describe the exact transformation of equation (1). Neglecting nonlinearity, one can find an exact linear solution of these equations with the initial conditions $\tau(0)=1$ and $\nu(0)=\nu_0$:

$$\tau^2=\frac{a^2+4[(a^2+4\nu_0^2)R(z)+\nu_0]^2}{a^2+4\nu_0^2};\quad \nu=\frac{(a^2+4\nu_0^2)R(z)+\nu_0}{\tau};\quad \frac{dR}{dz}=d(z). \tag{7}$$

When nonlinear effects and residual dispersion are negligible ($R(z_a)=R(0)=0$) the pulse recovers its original form. The combined action of the residual dispersion and nonlinearity modifies the periodic solutions (7), and they cannot be expressed in explicit form. Numerical periodic solutions of equations (4), (6) have been presented in Ref. 14. It should be pointed out that the nonlinearity and residual dispersion represent a small perturbation of the linear solution, and expression (7) can be used as a first approximation of the solution in the general case. As will be shown below, the structure of the equation describing the averaged dynamics does not depend on the specifics of the dispersion compensation scheme. However, the oscillatory behavior of the pulse given by $\tau(z)$ and $\nu(z)$ is determined, evidently, by the dispersion map. Substitution of (6) into (5) yields

$$iQ_z+\frac{d(z)}{\tau^2}[Q_{\xi\xi}-a^2\xi^2Q]+\frac{c(z)}{\tau}(|Q|^2Q+a^2\xi^2Q)=0. \tag{8}$$

Most of the dispersion maps $d(z)$ currently used in practice are built from pieces of fibers with different dispersion (negative or positive). Note that for such dispersion maps the condition $d^2>0$ is satisfied. Therefore, in what follows we consider only dispersion compensation schemes with $d^2>0$. This allows us to rewrite the coefficient in front of the last term in Eq. (8) as

$$\frac{c(z)}{\tau(z)}=\frac{d(z)}{\tau^2}\left[\frac{d(z)}{d^2}c(z)\tau(z)\right]\equiv\frac{d(z)}{\tau^2}\alpha(z'). \tag{9}$$

We introduce here a new variable $z'(z)$ defined through

$$\frac{dz'}{dz}=\frac{d(z)}{\tau(z)^2};\quad z'(0)=0. \tag{10}$$

After substitution of (9) and (10) into Eq. (8) we get

$$iQ_{z'}+Q_{\xi\xi}-a^2\xi^2Q+\alpha(z')(|Q|^2Q+a^2\xi^2Q)=0. \tag{11}$$

The variable z' oscillates rapidly and grows slowly over the amplification period in the case of anomalous residual dispersion. In the case of periodic τ and ν the function $z'(z)$ is the sum of a periodic function with zero mean value and a linearly growing part (due to residual dispersion). It is interesting to note that as a particular case (for a specific dispersion map), our general theory reproduces the results obtained in Ref. 18. Namely, for the special dispersion profile having a form

$$d(z)=\frac{ac(z)}{\sqrt{a^2+4\nu_0^2}}\cosh[2\sqrt{a^2+4\nu_0^2}y(z)];\quad \frac{dy}{dz}=c(z);$$

$$\cosh[2\sqrt{a^2+4\nu_0^2}y(0)]=\frac{\sqrt{a^2+4\nu_0^2}}{a}, \tag{12}$$

the function $\alpha(z')$ in Eq. (11) becomes a constant. For this specific choice of the dispersion profile Eq. (1) is transformed exactly to the NLSE with an additional quadratic potential.[18] However, the pulse chirp is not recovered after an amplification period in such a system, and an additional dispersion-compensating element should be added at the end of each section.

We now demonstrate that in the general case of an arbitrary dispersion map (under the conditions specified above), the average evolution of the pulse dynamics in Eq. (1) is given by the NLSE with an additional parabolic potential. An averaging procedure in the form of a Lie transform[16] or the method used in Ref. 19 can be applied directly to the transformed equation (11). In this letter we present the result only to leading order, because already in this order remarkable new properties of the average soliton arise. Averaging is over one cycle of the variation of z', corresponding to one amplification period. We use also the following useful relations (here $\oint$ denotes integration over one cycle in z')

$$\oint dz'=\int\frac{d(z)}{\tau^2}dz;\quad \oint\alpha(z')dz'=\int\frac{c(z)}{\tau}dz. \tag{13}$$

After straightforward calculations, the averaged equation describing the slow evolution of the chirped pulse due to nonlinearity and residual dispersion reads, to leading order,

$$i\frac{\partial U}{\partial z'}+\frac{\partial^2 U}{\partial \xi^2}-\left(1-\frac{r_1}{r_2}\right)a^2\xi^2 U+\frac{r_1}{r_2}|U|^2U=0;\quad r_1=\left\langle\frac{c}{\tau}\right\rangle;\quad r_2=\left\langle\frac{d}{\tau^2}\right\rangle. \tag{14}$$

Here $\langle f\rangle$ denotes averaging over one amplification period in z. This averaged equation is the main result of the present letter. This equation possesses a steady-state solution in the form of a soliton with Gaussian wings[14,18] in the case of a trapping potential $r_1/r_2<1$. Taking into account that the pulse form in the original variables is given by transformation (3), it is seen that an asymptotic pulse is highly chirped. In the case $r_1/r_2>1$ the effective potential is nontrapping. This leads to the tunneling of radiation through the barrier formed by the nonlinear term and the parabolic potential. Thus the average dynamics strictly depends on the value of the parameter r_1/r_2 that is determined by the dispersion map and system parameters. A comprehensive investigation of a soliton solutiuon of Eq. (14) will be published elsewhere. Higher order corrections to Eq. (14) can be found using the Lie transform technique developed in Ref. 16. Equation (14) is a Hamiltonian system:

$$i\frac{\partial U}{\partial z'}=\frac{\delta H}{\delta U^*};\quad H=\int|U_\xi|^2d\xi+\left(1-\frac{r_1}{r_2}\right)a^2\int\xi^2|U|^2d\xi-\frac{r_1}{2r_2}\int|U|^4d\xi. \tag{15}$$

A simple scaling analysis of the Hamiltonian indicates that the ground soliton solution of Eq. (14) is stable. It should be pointed out that if the input pulse differs from that of the soliton solution of equation (14), radiation will be emitted during the formation of the breathing soliton. Interaction of the soliton with the radiation gives rise to the slowly decreasing oscillations studied in the case of the NLSE in Ref. 21. As was found in Ref. 14 by numerical simulations of the original Eq. (1), in the general case the asymptotic state is a breathing soliton interacting with a radiative pedestal.

In conclusion, an averaged equation has been derived in leading order to describe the asymptotic breathing dynamics of a chirped optical pulse in transmission systems with dispersion compensation. This averaged equation is the NLSE with an additional quadratic potential. It is demonstrated that in the case of a trapping potential the breathing pulse shape is intermediate between the NLSE sech-type soliton and a Gaussian pulse. In the case of a nontrapping potential, the soliton emits radiation due to the tunneling effect.

I would like to thank I. Gabitov and A. Hasegawa for valuable discussions.

[a)]e-mail: tur@okibox.iae.nsk.su

[1] L. F. Mollenauer, P. V. Mamyushev, and M. J. Neubelt, Opt. Lett. **19**, 704 (1995); ''Demonstration of soliton WDM transmission at up to 8X10Gbit/s, error-free over transoceanic distances,'' Post Deadline presentation, PD22-1, OFC'96, San Jose.
[2] V. E. Zakharov and A. B. Shabat, Zh. Éksp. Teor. Fiz. **60**, 136 (1971) [Sov. Phys. JETP **33**, 77 (1971)].
[3] C. Desem and P. L. Chu, in *Optical Solitons—Theory and Experiment*, J. R. Taylor, ed., Cambridge University Press, 1992.
[4] N. S. Bergano *et al.*, Post Deadline presentation, PD23-1, OFC'96, San Jose.

[5] S. Artigaud *et al.*, Electron. Lett. **32**, 1389 (1996).
[6] C. Das *et al.*, Electron. Lett. **31**, 305 (1995).
[7] I. Gabitov and S. K. Turitsyn, Opt. Lett. **21**, 327 (1996); JETP Lett. **63**, 861 (1996).
[8] N. Smith, F. M. Knox, N. J. Doran *et al.*, Electron. Lett. **32**, 55 (1995).
[9] M. Nakazawa and H. Kubota, Jpn. J. Appl. Phys., Part 1 **34**, L681 (1995).
[10] J. M. Jacob, E. A. Golovchenko, A. N. Pilipetskii *et al.*, IEEE Photonics Technol. Lett. **9**, 130 (1997).
[11] J. C. Bronski and J. N. Kutz, Opt. Lett. **21**, 937 (1996).
[12] F. Kh. Abdullaev, S. A. Darmanyan, A. Kobyakov, and F. Lederer, Phys. Lett. A **220**, 213 (1996).
[13] B. Malomed, D. Parker, and N. Smyth, Phys. Rev. E **48**, 1418 (1993).
[14] I. Gabitov, E. G. Shapiro, and S. K. Turitsyn, Opt. Commun. **134**, 317 (1996); Phys. Rev. E **55,** 3624 (1997).
[15] N. J. Smith, N. J. Doran, F. M. Knox, and W. Forysiak, Opt. Lett. **21**, 1981 (1997).
[16] A. Hasegawa and Y. Kodama, Opt. Lett. **15**, 1444 (1990); Phys. Rev. Lett. **66**, 161 (1991).
[17] V. I. Talanov, JETP Lett. **11**, 199 (1970).
[18] S. Kumar and A. Hasegawa, Opt. Lett. **22**, 372 (1997).
[19] Yu. S. Kivshar, K. H. Spatschek, M. L. Q. Teixeiro, and S. K. Turitsyn, Pure Appl. Opt. **4,** 281 (1995).
[20] V. K. Mezentsev, E. G. Shapiro, and S. K. Turitsyn, to be published.
[21] E. A. Kuznetsov, A. V. Mikhailov, and I. A. Shimokhin, Physica D **87**, 281 (1995).

Published in English in the original Russian journal. Edited by Steve Torstveit.

Resonance tunneling via excited subbands and the existence of a new type of electric-field domains in long-period superlattices

Yu. A. Mityagin, V. N. Murzin, Yu. A. Efimov, and G. K. Rasulova
P. N. Lebedev Physics Institute, Russian Academy of Sciences, 117924 Moscow, Russia

(Submitted 23 April 1997)
Pis'ma Zh. Éksp. Teor. Fiz. **65**, No. 11, 818–822 (10 June 1997)

Successive resonance tunneling via excited states, accompanied by the appearance of resonance features on the multistability current–voltage branches, is observed in a superlattice. The data show a strongly nonequilibrium charge-carrier distribution over subbands with energies below the energy of an optical phonon and indicate that a new type of an electric-field domain forms, the structure of which is determined by resonance tunneling between excited subbands in neighboring quantum wells. © *1997 American Institute of Physics.*
[S0021-3640(97)00411-8]

PACS numbers: 78.66.−w, 73.40.Gk

It is well known[1] that resonance tunneling during transverse transport in weakly coupled superlattices (SLs) destroys the uniformity of the electric field and gives rise to regions with different values of the electric field and different resonance-tunneling structures (electric-field domains) in the SL. Current flow through a SL under these conditions is due to the so-called successive resonance tunneling, in which charge carriers from the bottom of the size-quantization subband in one quantum well tunnel into one of the top resonance subbands in a neighboring quantum well and then relax into the bottom subband in that well and then again tunnel into the next quantum well. Since the relaxation time (determined primarily by the emission of optical phonons) in weakly coupled superlattices is much shorter than the tunneling time, the population of the upper subbands is low, and the contribution of these subbands to the tunneling current is ordinarily neglected.

This letter presents data attesting to the observation of, together with tunneling from the bottom subband, resonance tunneling from excited size-quantization subbands. The effect was recorded in transverse-transport measurements in long-period superlattices with wide quantum wells and barriers in which several size-quantization subbands are present below the energy level of an optical phonon and the interband charge-carrier relaxation times, determined by scattering by impurities and acoustic phonons, become comparable to the tunneling time. It is shown that in this situation the charge-carrier distribution in the bottom sublevels deviates strongly from the equilibrium distribution. The data obtained attest to the appearance of domains of a new type, whose resonance-tunneling structure is determined by tunneling between the excited size-quantization subbands in neighboring quantum wells.

The experimental samples were grown by molecular-beam epitaxy and consisted of 30-period GaAs/AlGaAs superlattices, containing quantum wells 350 Å wide and with 120-Å barriers, between two heavily doped *n*-GaAs layers (2×10^{18} cm^{-3}). The superlattices were nominally undoped and possessed a residual donor impurity density of the order of 5×10^{15} cm^{-3}. The electrical measurements were performed on mesa structures with a 600 μm mesa diameter and Cr/Au contacts prepared by vacuum deposition. The measurements were performed at a temperature of 4.2 K.

The current–voltage characteristics (IVCs) obtained as a result of the transverse-transport measurements possessed the characteristic stepped form with several plateaus and an unmistakable small-scale periodic structure (negative differential conductivity (NDC) peaks) which are due to the formation of electric-field domains and the abrupt displacement of a domain wall through a sequence of quantum wells in the SL as the voltage applied to the SL is increased (or decreased).[2] Each plateau-like section of the IVC corresponds to the formation of a new domain in which resonance tunneling occurs into a state that is more highly excited than the rest of the superlattice, which possesses the resonance-tunneling structure of a domain with a weaker electric field, occurs. The period of the small-scale NDC oscillations approximately equals the energy splitting between the corresponding excited subbands of the strong- and weak-electric-field domains participating in the resonance tunneling. The observed current hysteresis (difference of the current values depending on the direction of sweep of the voltage applied to the SL) is due to the difference in the conditions of instability which determine the formation and deformation of the electric-field domains with increasing or decreasing voltage applied to the SL.[2]

These features are all displayed in Fig. 1a, which shows a fragment of the measured IVCs, for the voltage range corresponding to the formation of the domain 1–6 (corresponding to resonance tunneling from the first into the sixth size-quantization subband in neighboring quantum wells). In addition to these data, Fig. 1a also shows the observed current branches that arise when the direction of voltage sweep inside the regions of current hysteresis is reversed. These branches (of which there are approximately $N-1$, where N is the number of periods of the SL) represent stable current states which are determined by the change in the barrier transmission with increasing (or decreasing) voltage on the SL with a fixed position (localized in the SL) of the domain wall.[3] A more careful examination of Fig. 1a shows that the recorded multistability current branches possess structure, including structure in the form of additional plateau-like sections of an oscillatory type. This structure repeats in all branches. For the same direction of the voltage sweep, on all branches the observed additional plateau-like sections are characterized by the same electric current, which is appreciably higher in the case of sweep up than in the case of sweep down.

To interpret the results we employed a kinetic model of the formation of the electric-field domains in SLs.[2,4,5] Introducing for each period of the SL an average electric field E_i ($E_i=u_i/d$, where u_i is the voltage drop across the ith period of the SL) and electron density n_i in the ith well, the following kinetic equations can be written for the current density $J(U)$ and the charge-carrier density n_i on the axis of the SL (i is the number of the well):

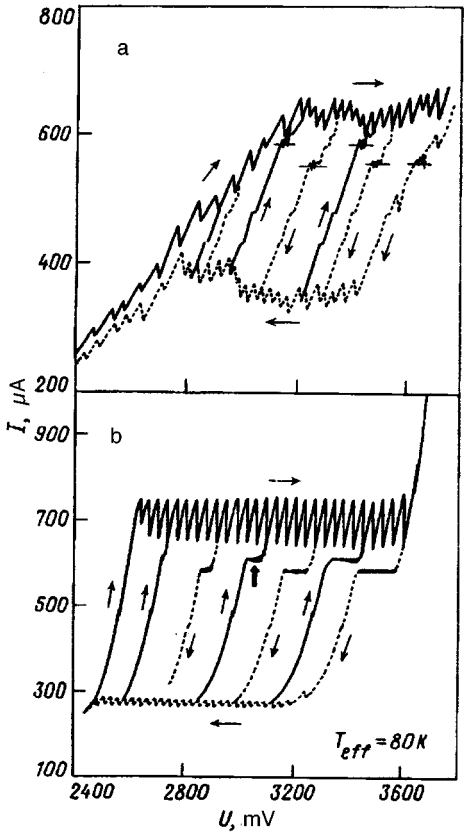

FIG. 1. a) Measured IVCs of GaAs/$Al_{0.3}Ga_{0.7}As$ ($d_w = 350$ Å, $d_b = 120$ Å) superlattices in the voltage range (1–6) corresponding to the formation of domains for upward (solid curve) and downward (dotted curve) sweeps of the voltage across the SL; b) computed IVCs for the same SL taking account of the resonance tunneling from excited subbands with $T_{\text{eff}} = 80$ K.

$$\frac{dn_i}{dt} = \frac{1}{d}[n_{i-1}v(u_{i-1}) - n_i v(u_i)], \tag{1}$$

$$(u_i - u_{i-1}) = \frac{4\pi e d}{\epsilon}(n_i - N_d), \tag{2}$$

$$\sum_{i=0}^{N} u_i = U, \quad J = \frac{\epsilon}{4\pi d}\frac{du_i}{dt} + \frac{e}{d}n_i v(u_i), \tag{3}$$

where d is the period of the SL, $v(u_i)$ is the tunneling drift velocity from the ith into the $(i+1)$-st quantum well, U is the voltage applied to the SL, and N_d is the donor impurity density (all donors are assumed to be ionized).

The stationary current–voltage characteristics as well as the electronic charge-carrier densities in the wells and the electric field profiles in the SL were calculated by solving Eqs. (1)–(3) numerically. The parameters appearing in the equations were determined by comparing the computed and measured IVCs (see Ref. 2 for details).

Effects due to tunneling from excited subbands are not included in Eqs. (1)–(3). To take such effects into account, we introduced the carrier distribution function over Boltzmann-type subbands with an effective temperature T_{eff}, which was treated as a parameter of the model. In this case we have the same equations (1)–(3) for n_i, $J(U)$, and E_i, once again treating n_i as the total electron density in the ith well but replacing the drift velocity function $v(u_i)$ by an effective drift velocity function

$$v_{\text{eff}}(u_i)=A\left(v(u_i)+\sum_{k=2}^{3} v\left(u_i-\frac{\Delta\epsilon_{1k}}{e}\right)\exp\left(-\frac{\Delta\epsilon_{1k}}{k_B T_{\text{eff}}}\right)\right), \tag{4}$$

where $\Delta\epsilon_{1k}=\epsilon_k-\epsilon_1$, ϵ_1, ϵ_2, and ϵ_3 are the energies of the subband minima and A is a normalization factor.

According to Eq. (4), at sufficiently high electric fields tunneling transitions from the second into the third subbands suppress the additional peaks in the function $v_{\text{eff}}(u_i)$. Figure 2a displays a fragment of the function $v_{\text{eff}}(u_i)$ for $T_{\text{eff}}=80$ K in the range of values of u_i corresponding to resonance tunneling between the subbands 1–5 and 1–6. One can see from the figure that the appearance of a quite pronounced additional peak in $v_{\text{eff}}(u_i)$, due to the tunneling transitions $2\rightarrow 6$, makes possible three stable values of u_i for the same value of the electric current, i.e., the SL can break up into three regions with different values of the electric field corresponding to the resonances $1\rightarrow 5$, $2\rightarrow 6$, and $1\rightarrow 6$. The computational results for the electric field strength and the spatial profile of the charge-density distribution presented in Figs. 2b and c confirm this. The appearance of a peak due to $2\rightarrow 6$ transitions leads to a splitting of the strong-electric-field domain $(2\rightarrow 6)$ into two regions, one of which is characterized by a weaker electric field and resonance tunneling of the $2\rightarrow 6$ type and the other by a stronger electric field and resonance tunneling of the $1\rightarrow 6$ type. The new domain wall formed by the additional space-charge layer is also clearly seen in Fig. 2b.

The computational results for the IVC taking account of tunneling between the excited subbands are presented in Fig. 1b. The good agreement between the theoretical and experimental data, including with respect to the additional observed plateau-like sections of the IVC with an oscillatory NDC structure, shows that the present study has yielded experimental proof for the appearance of electric-field domains of a new type, whose structure is determined by resonance tunneling from excited size-quantization subbands. The data obtained attest to a strongly nonequilibrium charge-carrier distribution in the lower subbands with energies less than the energy of an optical phonon in long-period superlattices in fields corresponding to tunneling into the upper subbands. Comparing the model calculations with the experimental data gives an effective temperature of the order of 100 K for the electronic subsystem in the SL in these fields, in complete agreement with the radiation measurements on intersubband transitions in similar superlattices.[6]

This work was supported by the Russian Fund for Fundamental Research under

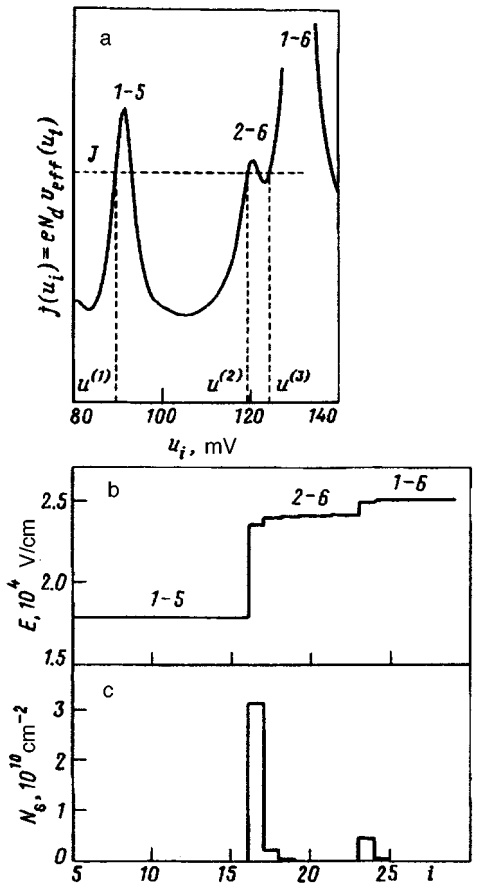

FIG. 2. Fragment of a model tunneling drift velocity function $v_{\text{eff}}(u_i)$ (a), profiles of the electric field (b), and space-charge distribution (c) calculated with allowance for tunneling from excited subbands for the current J and voltage U indicated by the thick vertical arrow in Fig. 1b.

Grant No. 96-02-18593, the Interdepartmental Scientific–Technical Program ''Physics of Solid-State Nanostructures'' under Grant No. 1-012, and INTAS under Grant No. 93-1704.

[1] L. Esaki and L. L. Chang, Phys. Rev. Lett. **33,** 495 (1974).
[2] Yu. A. Mityagin and V. N. Murzin, JETP Lett. **64,** 155 (1996).
[3] J. Kastrup, H. T. Grahn, K. Ploog *et al.*, Appl. Phys. Lett. **65,** 1808 (1994).
[4] F. Prengel, A. Wacker, and E. Scholl, Phys. Rev. B **50,** 1705 (1994).
[5] L. L. Bonilla, J. Galan, J. A. Guesta *et al.*, Phys. Rev. B **50**, 8644 (1994).
[6] M. Helm, P. England, E. Colas *et al.*, Phys. Rev. Lett. **63**, 74 (1989).

Translated by M. E. Alferieff

On low-field electron emission mechanisms

A. A. Dadykin
Institute of Physics, Ukrainian National Academy of Sciences, 252022 Kiev, Ukraine

(Submitted 11 March 1997; resubmitted 5 May 1997)
Pis'ma Zh. Éksp. Teor. Fiz. **65**, No. 11, 823–827 (10 June 1997)

It is established by direct experiments that the main component of the stationary field-emission current in fields $E<10^5$ V/cm is due to piezo-geometric intensification (by a factor of 10^3) of the electricfield at the end faces of piezoelectrically active films. An emission mechanism governed by electrons supplied by tunneling from the valence band of the piezoelectric is proposed. © *1997 American Institute of Physics.* [S0021-3640(97)00511-2]

PACS numbers: 77.65.−j, 79.70.+q

1. In investigations of field emission from metals and semiconductors, strong cold stationary electron emission is observed in average electric fields $\sim 10^5$ V/cm, two to three orders of magnitude lower than predicted by the theory. This phenomenon is known in the literature[1,2] as low-field electron emission (LFEE). LFEE is distinguished by high stability in a relatively low vacuum ($p>10^{-5}$ Torr) and high current density (>10 A/cm^2). This makes it attractive to develop a new generation of efficient electron sources, operating on the basis of this phenomenon, for various electronic devices, including bright cathodoluminescent flat panel displays. However, practical applications of the phenomenon are impeded by a lack of a clear understanding of the nature and mechanism of the phenomenon. The appearance of LFEE cannot be explained by a simple geometric intensification of the electric field and a decrease in the work function, since emission centers often appear both on the smooth side surface of tips and away from areas where the work function is depressed, for example, by the local implantation of sodium in polished wafers. In Refs. 3 and 4 LFEE is attributed, on the basis of photoemission data for the (III) face of diamond[5] and assuming different electron-supply mechanisms,[3] to the presence of sections with natural negative electron affinity (NEA) on the emitting surface. At the same time, according to the data in Ref. 6, natural NEA on the emitter surface is not at all necessary for appreciable LFEE: Efficient LFEE, and even more stable than in the case of diamond, is obtained from ZnS-type insulating films with an obviously positive electron affinity. Therefore the question as to the mechanism of the phenomenon remains open. In Ref.6, two forms of emission with substantially different time constants, current densities, and current–voltage characteristics are found, and the mechanism of the slow ($\tau>10^{-3}$ s) LFEE component is discussed. This mechanism is governed by electron injection from a metal substrate by tunneling through a narrow potential barrier in the presence of the built-in positive charge in the film. It is conjectured that the penetration of an external field into the emitter creates conditions for an effective NEA on its surface.

In the present letter it is found that the stationary fast ($\tau<10^{-7}$ s) LFEE is associ-

ated with the piezoelectric effect in samples of a special form, and an emission mechanism based on the Zener effect is proposed. The nonstationary[7] and exoelectronic[8] emission from ferroelectrics are also attributed to piezopolarization.

2. The experiments were performed with field-emission projectors and flat diode cells with different ($\sim 20\ \mu\text{m} \leqslant l \leqslant 1$ cm) cathode–anode distances. To visualize the emission, the anode was covered with a ZnS-type phosphor. The spatial distribution of the emission and the change occurring in the geometric relief of both cell electrodes in the course of the experiments were investigated with optical and scanning electron microscopes. The current–voltage and noise characteristics as well as the time constant of the emission from a separate (~ 100 Å) section of the cathode were studied by a correlation method,[9] which makes it possible to perform measurements in an electron-counting mode. The average electric fields at the emitter surfaces were estimated from the geometry of the test diodes. Emitters in the form of silicon and tungsten tips as well as plates and films made of quartz and other insulators (of the ZnS type) were fabricated and tested.

3. It was determined that LFEE arises on the cathode at locations of insulating film formations which have a quite large ratio (~ 100) of longitudinal dimensions l_2 to thickness l_1. These formations are oxide residues, which form during sample preparation and are difficult to remove, or films consisting of the sputtering products of the phosphor from the anode screen.

The slow LFEE with current density $\sim 10^{-3}$ A/cm^2 is distributed uniformly over the entire surface of the film formation. Its current–voltage characteristics[6] are similar to those of a dielectric diode operating in a regime when the current is limited by the space charge of ionized donor traps. The emission time constant is determined by the build-up time of this charge. Evidently, emission of this type should predominate in samples with a high density of defects; this is confirmed by control experiments with films prepared under different technological conditions.

The fast component, which for current density >10 A/cm^2 is concentrated at the locations of breaks in the film formations on the end faces of the film, makes the main contribution to the LFEE. The typical Fowler–Nordheim (FN) characteristic of this form of emission, possessing rectilinear sections with two different slopes, reflects an emission mechanism which is qualitatively different from that of the slow-LFEE mechanism.

If the slow emission is associated with defects in the emitter material, then with what property of the material is the fast component associated? The experiments showed that in all cases, without exception, the fast LFEE arises from the end faces of emitters whose material exhibits appreciable piezoelectric activity, and it can be conjectured that the appearance of this component is associated precisely with this property.

4. The most appropriate material for checking this hypothesis is quartz, whose piezoelectric properties have been well studied.[10] In the present work, commercial single-crystal skew Y-cut quartzpiezoelectric resonators in the form of disks with diameter $l_2 \sim 12.5$ mm and thickness $l_1 \sim 0.1$ mm, so that $l_2/l_1 \sim 100$, just as in the thin-film LFEE formations, were used as models of ''LFEE centers.''

Electrodes for applying a polarizing voltage $\pm V_1$ were deposited on the side surfaces of the disk, which was placed inside a cylindrical anode screen at voltage $+V_a$, by

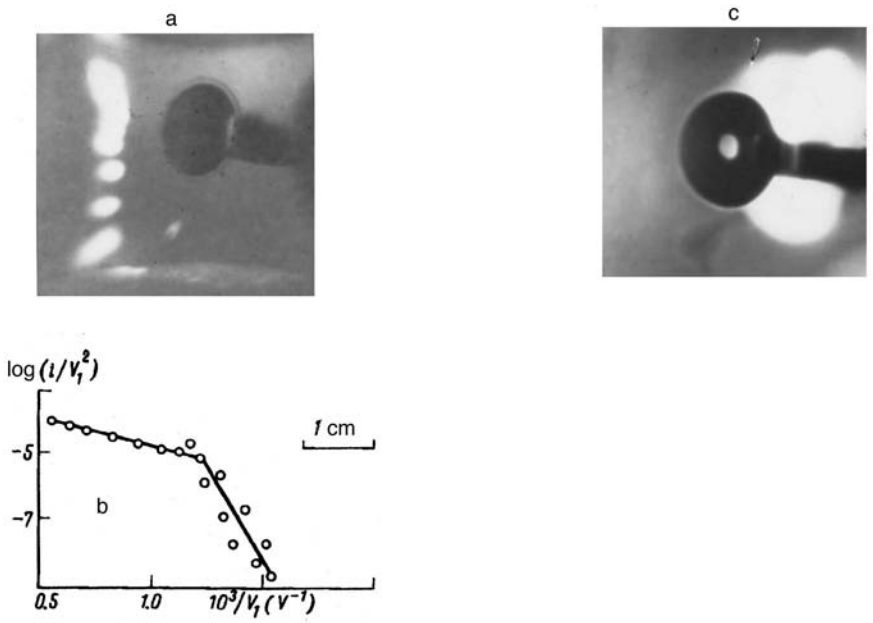

FIG. 1. a) Distribution of electron emission from a quartzpiezoelectric resonator: $V_1=4$ kV, $V_a=4$ kV. b) Typical FN characteristicof fast LFEE (disk with opening). c) Emission distribution in the case of a disk with an opening; $V_1=1$ kV, $V_a=4$ kV.

thermal vacuum sputtering. No emission was observed in the absence of a polarizing voltage, even with average electric fields exceeding 10^6 V/cm at the emitter surfaces.

Strong stationary emission ($j>10$ A/cm^2) from the end face of the disk was recorded even with a polarizing field $E_1=V_1/l_1<10^5$ V/cm. The exterior form of the emitter and the distribution of emission over its surface are displayed in Fig. 1a and a typical FN emission characteristic is displayed in Fig. 1b.

The emission image of the sample with variable polarity V_1 flips over in accordance with the orientation of the piezoelectrically active X axes of quartz, and as the magnitude of the voltage changes, the image rotates continuously in the plane of the disk, probably as a result of shear piezopolarization.

When the ratio l_2/l_1 is increased by halving the thickness of the disk, the emission voltages decrease by half.

Emission in a disk with an opening (Fig. 1c) is concentrated at the inner face with $E_1\sim10^4$ V/cm, in accordance with the decrease in the area of the emitting surface.

The results are also confirmed in cases of thin-film piezoelectrically active textures ZnO, ZnS, ZnSe, CdS, CdSe, AlN, and SiO_2 deposited on massive substrates. The textures were prepared in the form of matrices of piezoelectric elements ($l_2\sim100$ μm, $l_2\sim0.1$ μm), simulating the insulating formations described in Sec. 3. The film thickness l_1 was made large enough for piezoelectric properties to appear in the film and for conditions of effective NEA to be realized on its surface. LFEE arises from the ends of

the piezoelectric elements with polarizing fields $E_1 < 10^5$ V/cm. These fields were estimated, under the experimentally substantiated assumption that the density of surface electronic states in the film is low, from the geometry of the diode cell as $E_1 = V_a / l \cdot \epsilon$, where V_a is the voltage applied to the diode, l is the width of the cathode–anode vacuum gap, and ϵ is the permittivity of the film material. It should be noted that in matrices consisting of elements with different values of l_2 emission arises from the end faces of the elements with the highest ratio l_2 / l_1.

Emission was not observed, even for $E_1 > 10^6$ V/cm, in the case of films consisting of nonpiezoelectrically active Al_2O_3.

It follows from the results presented above that LFEE is due topiezopolarization and not a simple geometric intensification of the electric field.

5. Calculations of the emission characteristics of piezoelectric elements with high current densities must be performed by solving simultaneously the equations of electrodynamics and the theory of elasticity. This is an extremely complicated problem, especially in the case of thin films on massive substrates. However, the experiments showed surprisingly good agreement between the experimental emission characteristics and the characteristics predicted in the ''zero current'' approximation. This makes it possible to estimate very simply the electric fields at the end faces of the emitters.

A piezoelectric element with dimensions l_2 and l_1 when placed in an electric field E_1 oriented parallel to the electric axis deforms in such a way that

$$\Delta l_2 / \Delta l_1 = \sigma \cdot l_2 / l_1, \tag{1}$$

where Δl_1 and Δl_2 are the absolute deformations and σ is Poisson's ratio. The potentials on the side surfaces and endfaces of the piezoelectric element are different and are proportional to the absolute deformations. As a result of the presence of a potential difference between the end face and side surfaces, contact electric fields appear in the region near the end faces. The magnitude of these fields can be estimated as is done in the theory of Langmuir spots:

$$E \sim (V_2 - V_1)/l_1, \tag{2}$$

where V_2 is the potential of the end-face surface and V_1 is the potential of the side surface. For $l_2 \gg l_1$, with allowance for the electromechanical coupling constant k, which depends on the properties of the material and the construction of the piezoelectric element,[11] the field can reach values

$$E = 4\pi\sigma k^2 \frac{l_2}{l_1} E_1 = \Pi E_1. \tag{3}$$

Ordinarily, $\sigma \sim 0.5$, $k \sim 0.1$–0.8, and $l_2 / l_1 \sim 10$–10^3, so that the coefficient Π (which can be called the piezogeometric intensification factor for the electric field) at a polarizing field E_1 can reach values of 10^3 and higher, if the emitter geometry is taken into account. This means that for polarizing fields of the order of 10^5 V/cm, the electric field at the end face of a piezoelectric element can exceed 10^7 V/cm.

For external electric fields $E > 10^7$ V/cm and an emitter material with a low permittivity (< 10) and a high density of surface electronic states($< 10^{11}$ cm^{-2}) the electric

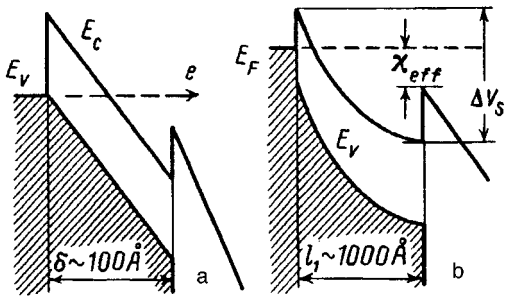

FIG. 2. Energy schemes with $\chi_{\text{eff}}=\chi-e\Delta V_s<0$: a) Fast piezoelectronic emission with $E>10^7$ V/cm; b) slow LFEE with $E<10^5$ V/cm; ΔV_s — change produced in the surface potential by the penetration of the electric field into the sample, χ — electron affinity of the emitter material, $\delta=\Delta V_s/E\epsilon$ —region of internal breakdown of the piezoelectric.

field reaches values in a surface region of width δ (Fig. 2a) that are high enough for internal electrical breakdown of the insulator (Zener effect). Such breakdown under the conditions for effective NEA at the surface, made possible by the penetration of the external field into the emitter, will determine the LFEE mechanism. It should be underscored that this mechanism of fast stationary field emission is possible only for piezoelectrics with sufficiently small ϵ. The energy scheme of a field emitter for this electron-supply mechanism is displayed in Fig. 2a (the energyscheme of slow LFEE is shown in Fig. 2b for comparison). In the scheme presented, the fast emission and its stability in a low vacuum seem obvious, since the ''electron source'' (valence band) is hidden from the external medium.

In summary, stationary LFEE can be described as a superposition of two current components with fundamentally different electron-supply mechanisms. In one case, when the density of donor traps in the film is high, the metal substrate acts as the electron source, while in the other case the electron source is the valence band of the piezoelectric. The second case, which was studied in the present letter, can be realized with materials which exhibit appreciable piezoelectric activity and are sufficiently perfect for a Zener effect to develop. In this connection, the most suitable name for emission of the form studied here could be ''piezoelectronic field emission.''

I am sincerely grateful to P. G. Borzyak for calling my attention to the problem of LFEE in emitters and to V. F. Kosorotov, A. G. Naumovets, O. G.Sarbeĭ, and B. V. Stetsenko for a number of important remarks and constructive suggestions which they made during a discussion of the experimental results. This work was supported by the Ukrainian State Committee on Science and Technology under Projects Nos. 2.3/242 and 06.01.00/234R-95.

[1] V. F. Babik, P. G. Borzyak, and A. F. Yatsenko, Ukr. Fiz. Zh. **13**, 868 (1968).
[2] K. H. Bayliss and R. V. Latham, Proc. R. Soc. London, Ser. A **403**, 285 (1986).
[3] N. S. Xu, Y. Tsong, and R. V. Latham, J. Phys. D. Appl. Phys. **26**, 1776 (1993).
[4] D. Hong and M. Aslam, Le Vide, les Couches Minces, Suppl. an N 271, 92 (1994).
[5] F. I. Himpsel, I. A. Knopp *et al.*, Phys. Rev. B **20**, 624 (1979).
[6] A. A. Dadykin, A. G. Naumovets, V. D. Andreev *et al.*, Diam. Relat. Mater. **5**, 771 (1996).

[7] O. Auciello, M. A. Ray, D. Palmer *et al.*, Appl. Phys. Lett. **66**, 2183 (1995).
[8] G. I. Rozenman and V. I. Pechorskiĭ, Pis'ma Zh. Tekh. Fiz. **6**, 1531 (1980) [Sov. Tech. Phys. Lett. **6**, 661 (1980)].
[9] A. A. Dadykin and A. G. Naumovets, Acta Phys. Pol. A **81**, 131 (1992).
[10] A. V. Shubnikov, *Selected Works on Crystallography* [in Russian], Nauka, Moscow, 1975.
[11] W. P. Mason, *Piezoelectric Crystals and Their Applications to Ultrasonics*, Van Nostrand, New York, 1950 [Russian translation, IL, Moscow, 1952].

Translated by M. E. Alferieff

Critical experiments in the search for fermion condensation

M. V. Zverev
Moscow Engineering-Physics Institute, 115409 Moscow, Russia; National Institute of Nuclear Physics (INFN), Catania, Italy

V. A. Khodel'
Kurchatov Institute Russian Science Center, 123182 Moscow, Russia

V. R. Shaginyan
St. Petersburg Institute of Nuclear Physics, Russian Academy of Sciences, 188350 Gatchina, Leningrad District, Russia

M. Baldo
National Institute of Nuclear Physics (INFN), Catania, Italy

(Submitted 5 May 1997)
Pis'ma Zh. Éksp. Teor. Fiz. **65**, No. 11, 828–833 (10 June 1997)

The specific features of fermion condensation — a phase transition associated with the rearrangement of the one-particle degrees of freedom in strongly correlated Fermi systems — by which this phenomenon can be detected experimentally are discussed. © *1997 American Institute of Physics.* [S0021-3640(97)00611-7]

PACS numbers: 05.30.Fk

Phase transitions of a new type, associated with the rearrangement of the single-particle degrees of freedom in strongly correlated Fermi systems, were predicted several years ago. An integral feature of this transition, called fermion condensation, is the appearance of a plateau in the single-particle excitation spectrum $\varepsilon_{\mathbf{p}}$ at the Fermi surface.[1–4] The plateau is associated with the fermion condensate (FC) and can arise in different systems, including quite unusual ones, for example, fermions locked in vortex cores in a superfluid Fermi liquid.[5] But the electronic systems of metals are apparently best suited for searching for such a condensate. The reason is that a method of making precise measurements of the single-particle electronic photoemission spectra has been developed in recent years for these systems.[6] It has been found that, surprisingly, these spectra (for example, the spectrum of $YBa_2Cu_4O_8$ (Ref. 7) or Sr_2RuO_4 (Refs. 8–10)) contain smooth segments on the Fermi surface which have not been reproduced in theoretical calculations.[11]

The specific nature of the FC lies in the unusual (linear) temperature dependence of its spectrum $\varepsilon_{\mathbf{p}}(T)$. This dependence is the ''calling card'' of the FC. How does it arise? Systems with a FC are described by singular solutions of the variational equation $\delta F/\delta n_{\mathbf{p}}(T)=0$ (Ref. 12; F is the free energy of the system), ordinarily rewritten in the form

$$n_{\mathbf{p}}(T)=\left\{1+\exp\frac{\varepsilon_{\mathbf{p}}[n]-\mu}{T}\right\}^{-1}, \tag{1}$$

where $\varepsilon_{\mathbf{p}}=\delta E_0/\delta n_{\mathbf{p}}$ is the quasiparticle energy, which itself depends on the quasiparticle distribution function $n_{\mathbf{p}}(T)$, and E_0 is the energy of the system and is a functional of $n_{\mathbf{p}}(T)$. In strongly correlated systems this dependence is very nontrivial, and this creates conditions for the appearance of singular solutions of equation (1).

In a homogeneous and isotropic system, where the spectrum $\varepsilon_{\mathbf{p}}$ depends only on the magnitude p of the momentum, a singular solution of Eq. (1) corresponding to a segment of the spectrum which is linear in T in the temperature interval $T_c<T<T_f^0$ has the form

$$\varepsilon_p(T)-\mu=T\nu_0(p)+O(T), \quad p_i<p<p_f. \tag{2}$$

The quantities T_c and T_f^0 will be determined below. For the time being, we set $T_c=0$. Outside the region occupied by the FC, the spectrum $\varepsilon_p(T)$ is essentially identical to the standard spectrum, for which the slope $d\varepsilon_p/dp>0$ at $T=0$ and varies quadratically as a function of T for $T>0$ (Ref. 13). This behavior of the spectrum outside the interval $p_i<p<p_f$ corresponds to the fact that outside this interval the singular solution is essentially identical to the standard solution. Indeed, $d\varepsilon_p(T=0)/dp\neq 0$, which at $T=0$ gives $n_0(p)=1$ for $p<p_i$ and $n_0(p)=0$ for $p>p_f$. Therefore the quasiparticle system separates into two subsystems — a normal subsystem with an effective mass M_F^* which does not depend on T, and the FC, whose effective mass, as follows from Eq. (2), is

$$M_{FC}^*\sim p_F(p_f-p_i)/T. \tag{3}$$

Here p_F is the Fermi momentum, related with the density of the liquid by the standard relation $\rho=p_F^3/(3\pi^2)$. Using Eq. (2), we find from Eq. (1) that $n_p(T)=n_0(p)+O(T)$, where $n_0(p)$ gives the momentum distribution of the FC at $T=0$:

$$n_0(p)=\{1+\exp(\nu_0(p))\}^{-1}, \quad p_i<p<p_f. \tag{4}$$

This is calculated from the equation $\delta E_0[n]/\delta n_0(p)=\mu$ (Ref. 1) under the assumption that the functional $E_0[n]$ is known. Knowing the distribution $n_0(p)$, one can calculate the spectrum ε_p from Eqs. (2) and (4), and, substituting expression (4) into the equation for the entropy,[12] one obtains a T-independent contribution

$$S_0=-\int_{p_i}^{p_f}[n_0(p)\ln n_0(p)+(1-n_0(p))\ln(1-n_0(p))]\frac{p^2dp}{\pi^2}, \tag{5}$$

which is proportional to the density of the FC

$$\rho_c=\int_{p_i}^{p_f}n_0(p)\frac{p^2dp}{\pi^2}. \tag{6}$$

This result also obtains directly from the Landau formula $S\sim p_F M^* T$ by substituting M_{FC}^* from Eq. (3).

Equation (5) remains valid when the damping γ of the condensate quasiparticles is taken into account. In Ref. 14 it was found that $\gamma(T)\sim T$. With the damping taken into account, the entropy S at low temperatures T is given by the formula[15]

$$S=\frac{2}{T}\int \varepsilon\frac{\partial n_F(\varepsilon)}{\partial\varepsilon}\ln\left(\frac{G_R(\mathbf{p},\varepsilon)}{G_R^*(\mathbf{p},\varepsilon)}\right)\frac{d\varepsilon d^3p}{(2\pi)^4 i}, \tag{7}$$

where $G_R(\varepsilon,\mathbf{p})=1/(\varepsilon-\varepsilon_p+i\gamma)$ is the retarded Green's function. After substitution of zT for ε in Eq. (7) the temperature T vanishes from the integral over the condensate region, since the spectrum $\varepsilon_p\sim T$ and the damping $\gamma\sim T$, and the same estimate $S_{FC}\sim\rho_c$ is obtained. Therefore the ratio S_{FC}/S_F of the entropy of the FC to the entropy of the rest of the system is very large at low temperatures T — it is proportional to $M_{FC}^*/M_F^*\sim\varepsilon_F/T$, where ε_F is the Fermi energy. We note that since S_0 does not contribute to the specific heat $C(T)=TdS/dT$, there is no such enhancement in $C(T)$.

A plateau adjacent to the Fermi surface has even been observed in the electronic spectra of some strongly correlated metals,[7–10] but the accuracy of the measurements is still too low to confirm or rule out a linear variation of $\varepsilon_{\mathbf{p}}(T)$ as a function of T. On the other hand, the existence of the T-independent condensate contribution S_0 associated with this behavior of the spectrum to the entropy in the interval $T_c<T<T_f^0$ can be checked experimentally by measuring the thermal expansion coefficient

$$\alpha=\frac{1}{3}\left(\frac{\partial\ \log V}{\partial T}\right)_P=-\frac{1}{3K}\rho\left(\frac{\partial(S/\rho)}{\partial\rho}\right)_T, \tag{8}$$

where $K=\partial P/\partial\rho$ is the compressibility of the system, P is the pressure, and V is the volume. Substituting into Eq. (8) expression (5) for the entropy, we find for the thermal expansion coefficient $\alpha_{FC}(T)$ of a system with a fermion condensate

$$\alpha_{FC}=\frac{1}{3K\rho}\left[S_0-\rho\int\frac{dn_0(p)}{d\rho}\ln\frac{1-n_0(p)}{n_0(p)}\right]\frac{p^2dp}{\pi^2}. \tag{9}$$

Hence follows the estimate $|\alpha_{FC}(T)|\sim\rho_c/(K\rho)$. At the same time, in a normal Fermi liquid this coefficient is of the order of $|\alpha_n|\sim M_F^*T/p_F^2K$. Neglecting the difference in the compressibilities K of these systems ($\delta K/K\sim\rho_c/\rho$; Ref. 14) gives for $|\alpha_{FC}/\alpha_n|$ the estimate

$$\left|\frac{\alpha_{FC}(T)}{\alpha_F(T)}\right|\sim\frac{M_{FC}^*}{M_F^*}\sim\frac{\rho_c}{\rho}\frac{p_F^2}{M_F^*T}\sim\frac{\rho_c}{\rho}\frac{\varepsilon_F}{T}. \tag{10}$$

We see that the ratio $|\alpha_{FC}(T)/\alpha_n(T)|$ is increased by the factor ε_F/T, and therefore a study of thermal expansion at low temperatures T can detect even low concentrations of a FC. It is worth noting that the increase in $\alpha(T)$ associated with the FC will also reveal itself in the difference $(C_P(T)-C_V(T))$, which is proportional to $T\alpha^2(T)$.[13]

The upper limit T_f^0, up to which these simple though unconventional relations hold, is determined by the rate of growth of the correction terms in Eq. (2) with increasing T: For $T\simeq T_f^0\simeq(p_f-p_i)^2/M$ they are of the same order of magnitude as the leading term. The results (2)–(5) must, unavoidably, be modified even in the limit of zero temperature, since the presence of a term $S_0\neq 0$, which is due to the degeneracy of the spectrum (2), at $T=0$ is incompatible with the Nernst theorem. The unbounded growth of the density of states has the effect that there are many possibilities for one of the Pomeranchuk conditions to be violated, and for this reason as $T\to 0$ the FC serves as a source for new

phase transitions which lift the degeneracy of the spectrum $\varepsilon_p(T)$ as $T\to 0$ and thereby eliminate S_0. Which phase transition dominates in reality and the importance of the contribution of the incoherent part of the effective interaction of the quasiparticles largely depend on the input-parameter game. We shall analyze below the situation when Cooper pairing wins the competition with other transitions. The quantity T_c in this case is determined by the temperature of the superconducting phase transition. As we shall see, the FC substantially changes the results of the BCS theory, deviations from whose predictions are often observed experimentally in strongly correlated metals.

Let us assume that $T_c < T_f^0$. Then below the phase-transition point the quasiparticle distribution $n_p(T)$ varies relatively little and the results (2)–(5) can be used as a zeroth approximation for constructing a new low-temperature expansion. In so doing, it should be kept in mind that the equation for the entropy S of a superfluid system with a fermion condensate must be written in the standard Bogolyubov form. Then $\lim_{T\to 0} S=0$ (Refs. 1, 3, and 13). The fact that S_0 vanishes on the T_c interval yields an estimate for the specific heat $C_s(T)$ of the superfluid phase in the region $T\sim T_c$: $C_s(T\leqslant T_c)\sim S_0/T_c$, which is much higher than the specific heat C_n of the normal phase at temperatures $T\geqslant T_c$. This should be manifested in the magnitude of the jump in $C(T)$ at the phase transition point; this jump is given by the equation[13]

$$C_s(T_c)=C_n(T_c)-\frac{1}{T_c}\int n_p(T_c)(1-n_p(T_c))\left(\frac{\partial\Delta_p^2}{\partial T}\right)_{T_c}\frac{p^2dp}{\pi^2}. \tag{11}$$

To find $\partial\Delta_p^2/\partial T$ we take into consideration the fact that the equation for the gap $\Delta_p(T)$ in the problem with the FC can have the same form as in the BCS theory:[1,3,13]

$$\Delta(p,T)=-\int V(p,p_1)\kappa(p_1,T)\tanh\frac{E(p_1,T)}{2T}\frac{p_1^2dp_1}{4\pi^2}, \tag{12}$$

where $\kappa(p,T)=\Delta_p(T)/2E(p,T)$ and $V(p,p_1)$ is a relatively weak attractive, strongly momentum-dependent potential. This dependence has the effect that $\Delta(p)$ is tied to the regions occupied by the FC (the corresponding calculations will be published in a separate work). At the same time, as analysis of expression (12) shows, in a system with a FC the dependence of the gap Δ_p on T near T_c is the same as in the BCS theory: $\Delta^2(T)\simeq\Delta^2(0)(1-T/T_c)$. This gives the estimate $-(\partial\Delta_p^2/\partial T)_{T_c}/T_c\sim 1$. The main feature of the situation considered here is that the integration in Eqs. (11) and (12) extends over the condensate region, a specific result of which is that the logarithmic divergence characteristic for the BCS theory does not appear here. This results in a suppression of the isotope effect in T_c, which in the BCS theory is attributed to the change in the Debye phonon frequency, as was shown in Ref. 16, where the experimental single-particle spectrum, with a plateau of the type (2), was used to solve the equation for the gap in high-T_c superconductors. The lack of an appreciable isotope effect in T_c serves as a necessary condition for the existence of a FC.

In a system with no FC the integral (11) is proportional to T_c: This is the volume of the region of integration close to the Fermi surface. In a system with a FC the integration in Eq. (11) extends over the region occupied by the fermion condensate, whose volume is

virtually independent of T_c ($\sim T_c/T_f^0$), and the result is proportional to the density ρ_c of the condensate. Ultimately, approximately the same enhancement is obtained for the ratio $C_s(T_c)/C_n(T_c)$ as for the thermal expansion coefficient

$$\frac{C_s(T_c)}{C_n(T_c)} \sim \frac{M_{FC}^*}{M_F^*} \sim \frac{\rho_c}{\rho}\frac{\varepsilon_F}{T_c}. \tag{13}$$

Equation (13) was obtained on the assumption that $\Delta_p(T \sim T_c)$ is nonvanishing in the entire region occupied by the FC. In the opposite case, ρ_c must be interpreted as the volume where $\Delta_p \neq 0$.

We note that the product $n_p(1-n_p)$ also appears in the width of the nuclear magnetic resonance line due to the scattering of conduction electrons by a polarized nucleus.[17] The same differences that were just mentioned should also be observed in these experiments — the linewidth in systems with a FC should contain a slightly T-dependent term.

The presence of a plateau in the spectrum (2) at $T=0$ is also manifested in an important effect: It causes the gain δE_s to depend on the pairing. This is seen even in the fact that the logarithmic divergence characteristic of the BCS theory does not occur in the case of the FC, and the gap Δ in Eq. (12) is linear in the coupling constant. Taking the variation of the occupation numbers as a function of the pairing to be a small correction, the gain in energy per particle $\delta E_s(T=0)$ can be estimated as[14]

$$\delta E_s(T=0) \simeq \Delta(0)\frac{\rho_c}{\rho}, \tag{14}$$

which is much greater than $\delta E_{BCS} \sim \Delta^2(0)/\varepsilon_F$. Although this result was obtained in Ref. 14 for the Nozières model,[3] it is a general result. This can be easily shown as follows. The equation for $\delta E_s(T=0)$ is obtained from the well-known Landau formula by adding a pairing contribution and has the form

$$\delta E_s(T=0) = \int \left[(\varepsilon_p - \mu)\delta n_0(p) - \frac{1}{4}\Delta(p)\kappa(p) \right] \frac{p^2 dp}{\pi^2}. \tag{15}$$

Here ε_p is calculated in a system without pairing, and δn_0 is the difference of the occupation numbers in superfluid and nonsuperfluid systems with a FC. In the standard case the first and second terms in the integrand in Eq. (15) almost completely compensate one another. In a system with a FC the first term vanishes and the second term — the integral over the region of the FC — remains and gives expression (14). Taking the term $\sim f\delta n \delta n$ into account does not change this result. Therefore in a system with a FC δE_s is linear while δE_{BCS} is quadratic in the gap width $\Delta(0)$. This enhancement has the effect of increasing the critical magnetic fields H_c at which superfluidity is destroyed in systems with a FC and of substantially altering the Ginzburg–Landau equations; this will be examined separately.

To apply the results obtained above to real metals, the anisotropy produced by the crystal field of the lattice must be taken into account. This refers chiefly to the structure of the condensate solution. As shown in Ref. 18 for the example of the exactly solvable Nozières model,[3] in a crystalline system a FC arises near the van Hove points, where the

velocity of the quasiparticles vanishes, and this in turn sharply increases their role and the magnitude of the anisotropic corrections. This result is independent of the form of the model interaction; only the presence of an appreciable velocity component of the forces is important. The sharp anisotropy of the gap leads to a unique variation of the specific heat — a significant fraction of the Fermi surface occupied by normal quasiparticles is almost pairing-free, as result of which a nonexponential term appears in $C(T)$ at temperatures much below T_c.

The oxide Sr_2RuO_4 — a substance with an almost square two-dimensional lattice and three single-particle bands near the Fermi surface — is most interesting from the standpoint of fermion condensation. The Fermi energy for this oxide is $\varepsilon_F \sim 1$ eV and at the same time $T_c \sim 1$ K, which creates unique conditions for detecting a FC ($\varepsilon_F / T_c \sim 10^4$). Recent data[8–10] show that a quite wide plateau extending in both directions appears in the spectrum $\varepsilon_{\mathbf{p}}$ of one of the bands near the Fermi surface, and the area of the plateau reaches 3% of the Brillouin zone. However, this ''pot of honey'' has a ''ladle of tar'' in connection with the referencing of the plateau. At first it was located 17 meV below the Fermi surface,[8] but now experimenters[10] place this plateau 11 meV from it, despite the fact that the energy resolution is around 15 meV. This result is dictated by the fact that the Fermi surface ordinarily lies at points where $n(p_F) = 1/2$. However, calculations show that while such referencing is valid in the normal case, it no longer operates in a system with a developed FC, and, furthermore, because of the extent of the plateau in momentum space it is difficult to eliminate the background, the parameters of whose variation along the plateau are nowhere to be found. Furthermore, such referencing, which signifies that one of the bands drops out of the game, does not agree at all with the specific heat data and the data on the de Haas–van Alphen effect.[19] In our view, better data on this effect together with measurements of the thermal expansion coefficient as well as the jump in the specific heat at the point T_c and the variation of C_P and C_V for $T < T_c$ could shed light on the nature of the remarkable properties of this oxide and on the whether or not fermion condensation is connected with them.

Thus we have analyzed some specific features of fermion condensation, including the flattening of the single-particle excitation spectrum at the Fermi surface with a characteristic linear temperature dependence of the slope $d\varepsilon_{\mathbf{p}}/dp$ of the spectrum as well as the thermal expansion coefficient, the jump in the specific heat at the phase transition point, and other characteristics. Since the properties of systems with a FC are radically different from those of standard systems, there is hope that measurements of these characteristics will make it possible, in the not too distant future, to determine whether or not this phenomenon is realized in strongly correlated metals.

We are grateful to G. E. Volovik, R. O. Zaĭtsev, N. E. Zeĭn, A. I. Likhtenshteĭn, R. Pucci, C. A. Swenson, and P. Schuck for helpful discussions. This work was supported by the Russian Fund for Fundamental Research under Grants Nos. 95-02-04481 and 96-02-19292.

[1] V. A. Khodel' and V. R. Shaginyan, JETP Lett. **51**, 553 (1990).
[2] G. E. Volovik, JETP Lett. **53**, 222 (1991).
[3] P. Nozières, J. Phys. I **2**, 443 (1992).
[4] V. A. Khodel, V. R. Shaginyan, and V. V. Khodel, Phys. Rep. **249**, 1 (1994).
[5] G. E. Volovik, JETP Lett. **63**, 763 (1996).

[6] Z.-X. Shen and D. S. Dessau, Phys. Rep. **253**, 1 (1995).
[7] K. Gofron *et al.*, J. Phys. Chem. Solids **54**, 1193 (1993).
[8] T. Yokoya *et al.*, Phys. Rev. Lett. **76**, 3009 (1996).
[9] D. H. Lu, M. Schmidt, T. R. Cummins *et al.*, Phys. Rev. Lett. **76**, 4845 (1996).
[10] T. Yokoya *et al.*, Phys. Rev. B **54**, 13311 (1996).
[11] D. J. Singh, Phys. Rev. B **52**, 1358 (1995).
[12] L. D. Landau, Zh. Éksp. Teor. Fiz. **30**, 1058 (1956) [Sov. Phys. JETP **3**, 920 (1956)].
[13] L. D. Landau and E. M. Lifshitz, *Statistical Physics*, Pergamon Press, New York [Russian original, Nauka, Moscow, 1976].
[14] J. Dukelsky, V. A. Khodel, P. Schuck, and V. R. Shaginyan, Z. Phys. B **102**, 245 (1997).
[15] A. A. Abrikosov, L. P. Gor'kov, and I. E. Dzyaloshinskiĭ, *Methods of Quantum Field Theory in Statistical Physics*, Prentice-Hall, Englewood Cliffs, N. J., 1963 [Russian original, Fizmatgiz, Moscow, 1962].
[16] A. A. Abrikosov, J. C. Campuzano, and K. Gofron, Physica C **214**, 71 (1993).
[17] A. P. Kampf, Phys. Rep. **249**, 219 (1995).
[18] G. E. Volovik, JETP Lett. **59**, 830 (1994).
[19] A. P. Mackenzie, S. R. Julian, A. J. Diver *et al.*, Phys. Rev. Lett. **76**, 3786 (1996).

Translated by M. E. Alferieff

Low-temperature resistivity of $YBa_2Cu_3O_{6+x}$ single crystals in the normal state

V. F. Gantmakher,[a] D. A. Pushin, D. V. Shovkun, and G. E. Tsydynzhapov
Institute of Solid State Physics, Russian Academy of Sciences, 142432 Chernogolovka, Moscow Region, Russia

L. P. Kozeeva and A. N. Lavrov[b]
Institute of Inorganic Chemistry, Siberian Branch of the Russian Academy of Sciences, 630090 Novosibirsk, Russia

(Submitted 15 May 1997)
Pis'ma Zh. Éksp. Teor. Fiz. **65**, No. 11, 834–839 (10 June 1997)

A scan of the superconductor–nonsuperconductor transformation in single crystals of $YBa_2Cu_3O_{6+x}$ ($x\approx 0.37$) is done in two alternative ways, namely, by applying a magnetic field and by reducing the hole concentration through oxygen rearrangement. The in-plane normal-state resistivity ρ_{ab} obtained in the two cases is quite similar; its temperature dependence can be fitted by a logarithmic law in a temperature range of almost two decades. However, an alternative representation of the temperature dependence of $\sigma_{ab}=1/\rho_{ab}$ by a power law, typical for a 3D material near a metal–insulator transition, is also plausible. The vertical conductivity $\sigma_c=1/\rho_c$ followed a power law, and neither $\sigma_c(T)$, nor $\rho_c(T)$ could be fitted by log T. It follows from the ρ_c measurements that the transformation at $T=0$ is split into two transitions: superconductor–normal-metal and normal-metal–insulator. In our samples, they are separated in oxygen content by $\Delta x\approx 0.025$. © *1997 American Institute of Physics.* [S0021-3640(97)00711-1]

PACS numbers: 72.15.Rn, 61.50.Ah, 74.62.Bf, 71.30+h

In this paper we intend to apply the scaling theory of localization[1] to the underdoped system $YBa_2Cu_3O_{6+x}$. The theory[1] allows one to classify the temperature dependence of the conductivity in the close vicinity of the metal–insulator transition in a 3D material. There is a critical region near the transition in which the conductivity $\sigma(T)$ follows a power law

$$\sigma=\alpha+\beta T^m. \tag{1}$$

When the main inelastic processes in the critical region are controlled by the electron–electron interaction, the exponent $m=1/3$ (Refs. 2 and 3). The constant α in the relation (1) is negative, $\alpha<0$, and the critical region there is bounded from below by a crossover temperature T^* on the insulating side of the transition. Below T^*, the conductivity falls off exponentially:[4,5]

$$\sigma \propto \exp[-(T_0/T)^n], \quad n=1,\ 1/2,\ \text{or}\ 1/4. \tag{2}$$

The crossover temperature T^* and the constant α both become zero at the transition point, so that $\sigma(T)$ at this point is proportional to $T^{1/3}$ (Refs. 2 and 3):

$$\sigma = \beta T^{1/3}. \tag{3}$$

This relation can be used for detecting the transition point.

A low-temperature crossover line exists in the critical region of the transition on the metallic side too. The conductivity here is described by dimensionless equation[6]

$$s^{3/2} = s^{1/2} + t^{1/2}, \quad s = \sigma(T)/\sigma(0), \quad t = T/T^*. \tag{4}$$

The function $s(t)$ goes over to the power laws (1) in the opposite temperature limits, with $\alpha = \sigma(0)$ and $m = 1/2$ at low temperatures, when $t \ll 1$, and with $\alpha = \frac{2}{3}\sigma(0)$ and $m = 1/3$ when $t \gg 1$. It follows from Eq. (4) that at the crossover temperature, when $t = 1$, the conductivity is $\sigma(T^*) = 1.75\ \sigma(0)$.

According to the theory,[1] a normal-metal–insulator transition does not exist in 2D materials: any film is expected to become insulating at $T = 0$. With decreasing temperature, the localization starts with the so called quantum corrections to the classical conductivity σ_0:

$$\sigma = \sigma_0 + \Delta\sigma = \sigma_0 + \gamma_\sigma \log T, \quad \Delta\sigma \ll \sigma_0. \tag{5}$$

The relation $\Delta\sigma < \sigma_0$ cannot be violated because the conductivity $\sigma(T)$ is always positive. When σ_0 and $\Delta\sigma$ become comparable, the weak localization turns into strong localization and the logarithmic behavior (5) gives way to the exponential behavior (2): at low enough temperature $\sigma(T)$ should fall off exponentially.

When the metal is superconducting the pattern of the transition to the insulating state changes. In 2D the superconductor–insulator transition has been observed experimentally.[7] In 3D it is not clear whether such a transition can take place as a single transition or whether it would occur through a normal-metal intermediate state. In order to study the low-temperature behavior of a superconductor, one can bring it to the transition, suppress the superconductivity by a magnetic field H, and then investigate the transition and its vicinity with the field held constant. It had been assumed that a material with supressed superconductivity would behave at finite temperatures as an ordinary metal. However, since 1980 there have been repeated experimental indications that fpr superconducting materials there is an intermediate region in the vicinity of the transition in which the normal resistivity varies logarithmically with temperature:[8]

$$\rho(T) = \rho_0 + \Delta\rho = \rho_0 - \gamma_\rho \log T. \tag{6}$$

The temperature dependence (6) has been found in granular aluminum[8] and granular niobium nitride films,[9] in percolating lead films,[10] and in $Nd_{2-x}Ce_xCuO_{4-y}$ ceramics.[11] In all these cases the resistance changes severalfold over the range of the logarithmic temperature dependence, the logarithmic term in (6) becoming the leading one at low temperature:

$$\Delta\rho \gg \rho_0. \tag{7}$$

Hence relation (6) cannot be converted into (5) despite the formal resemblance between them.

Interest in this problem has been renewed after the publications by Ando, Boebinger, *et al.*,[12,13] which revealed the $\log T$ term in the resistivity of underdoped $La_{2-x}Sr_xCuO_4$ in pulsed magnetic fields of 60 T. This interest has several aspects.

(i) As the volume of experimental data is rather poor, one cannot be confident and must check whether the $\log T$ term really exists — it is not simple nor even always possible to distinguish between $\log T$ and a power-law dependence (1).

(ii) What are the specific properties of those materials for which this term appears? If these should turn out to be exclusively high-T_c superconductors[11–14] it would point to a specific role of strong correlations in electron systems; on the other hand, it may turn out that it is granularity which is of primary importance.[8–11,14]

Motivated by these goals, we present below the measurements of the temperature dependence of the in-plane ρ_{ab} and vertical ρ_c resistance of the single crystals $YBa_2Cu_3O_{6+x}$. By decreasing the doping level in high-T_c superconductor systems, one can suppress the superconducting transition temperature T_c and bring the system to the boundary of the superconducting region. In the YBaCuO system this can be done by decreasing the oxygen content or, in a limited range, by oxygen rearrangement in the planes of CuO chains.[15,16]

Single crystals of $YBa_2Cu_3O_{6+x}$ were grown by the flux method in alumina crucibles.[17] Oxygenated at 500 °C in flowing oxygen, they had a T_c of about 90–92 K and a fairly narrow resistive transition $\Delta T_c < 1$ K. To bring the samples to the boundary of the superconducting region, the oxygen content was reduced by high-temperature (770–820 °C) annealing in air with subsequent quenching in liquid nitrogen.[16,17] To rearrange the chain-layer oxygen subsystem, the $YBa_2Cu_3O_{6+x}$ crystal was heated to 120–140 °C and quenched in liquid nitrogen. This procedure reduces the mean length of the Cu–O chains; hence, the hole doping of CuO_2 planes decreases.[18,19] The equilibrium state, with a larger hole density, can be restored simply by room-temperature aging. By dosing the aging time, one can also obtain intermediate states. Thus the quenching–aging procedure allows one to vary gradually the charge carrier density and to tune the sample state through the boundary of the superconducting region.

Special care was taken to measure reliably the separate resistivity components. The in-plane resistivity was measured on thin (20–40 μm thick) plate-like crystals by the four-probe method with current contacts covering two opposite lateral surfaces of the crystal.[17] The contacts were painted on with silver paste and were fixed by annealing. To measure the vertical resistivity, circular current electrodes were painted on the opposite sides of the plate, with potential probes in the middle of the circles. The resistivity was measured by the standard low-frequency (23 Hz) lock-in technique in the temperature range 0.37–300 K, the measuring current being low enough to avoid any sign of sample overheating even at the lowest temperature.

Below we present the temperature dependence of the in-plane resistivity obtained for the ''aged'' and ''quenched'' states of one of the $YBa_2Cu_3O_{6+x}$ ($x \approx 0.37$) crystals. For both states the resistivity passed through a minimum near 50 K. The ratio r of the resistance at room temperature to that at minimum was ≈ 3. (In terms of classical metal physics this means that the crystal is not perfect: crystals for which $r \approx 10$ do exist.) In the quenched state, no signs of the superconducting transition were observed on the $\rho(T)$

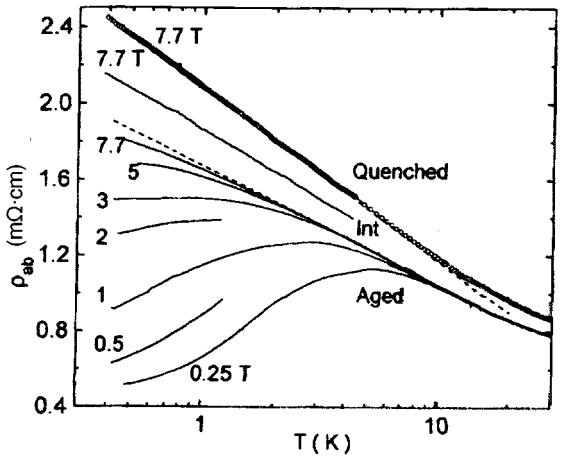

FIG. 1. In-plane resistivity versus log T for a YBaCuO single crystal with a fixed oxygen content but with different oxygen arrangements (quenched, intermediate, and aged states). Only the aged state is superconducting, and the set of curves demonstrates how a field $\mathbf{H}\|c$ destroys the superconductivity. The dashed lines are an extrapolation of the linear dependence $\rho_{ab}(\log T)$. Experimental points are plotted only on one curve.

curve down to the lowest temperature. In the aged state, the resistivity growth at low temperatures was interrupted by the superconducting transition. Owing to the low $T_c < 10$ K, the superconducting transition could be suppressed almost completely by the available magnetic field $\mathbf{H}\|c$.

Attempts to fit the $\rho_{ab}(T)$ data by an exponential law (2) were unsuccessful. On the contrary, we succeeded in fitting the data by the logarithmic law (5); see Fig. 1. The quenched and the intermediate states, which both lack superconductivity, exhibited a resistivity which increased logarithmically with decreasing T over almost two decades of temperature. The magnetoresistance of the quenched state was below 1%; thus the perfect fit demonstrated in Fig. 1 obtains both with and without a magnetic field. It can be seen that with increasing magnetic field the $\rho_{ab}(T)$ curves for the aged state make a step-by-step approach to a straight line. Apparently the deviations from the logarithmic law (5) indicate only that the highest applied field 7.7 T was not strong enough. Thus the representation of the data given in Fig. 1 agrees with that of Refs. 11–14.

However, this is not the only possible interpretation. Assuming that our sample is a 3D material, we can analyze the data with the help of Eqs. (1) and (4). According to Fig. 2, the data for the quenched state of the sample, replotted as σ versus $T^{1/3}$, approach a straight line at large T and satisfy Eq. (4) with the parameter values $\sigma(0) = 0.23$ MS/cm and $T^* = 0.37$ K. The values for the intermediate state are $\sigma(0) = 0.32$ MS/cm and $T^* = 1.25$ K. Thus this approach is self-consistent: the aging of the sample increases the hole density and thereby leads to an increase of the conductance $\sigma(0)$ and crossover temperature T^*.

Therefore, at this stage we cannot choose between the log T and T^m representations, i.e., between representations (5) and (1), (4). We have done experiments on a crystal with $r \approx 10$, too, but were left with the same uncertainty. However, in any case the supercon-

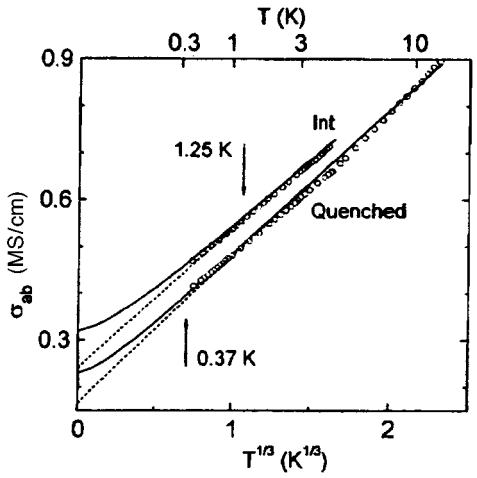

FIG. 2. The data for quenched and intermediate states from Fig. 1 replotted as σ_{ab} vs $T^{1/3}$. Solid lines – fits by Eq. (3) with the T^* values indicated by arrows, dashed lines – asymptotes in the $t \gg 1$ region.

ducting state does not give way directly to an insulator: representation (5) would indicate that it converts into some specific strongly correlated metallic state, while representation (1) would point to a normal-metal state. The conclusion that the transformation in YBaCuO consists of two stages: into normal metal first and into insulator after further decrease of the hole density, was made previously[20] on the basis of an extrapolation of the transport data from high temperatures (from above the resistance minimum). Here the extrapolation edge is far lower — only 0.4 K.

The transport properties of YBaCuO crystals near the boundary of the superconducting region are highly anisotropic, the ratio ρ_c/ρ_{ab} exceeding 10^3 (Ref. 21). The crystals can be regarded as a stack of weakly bound conducting CuO_2 planes. This brings some uncertainty to the question of whether the in-plane transport should be considered to be of a 2D or of 3D type. At the same time the vertical transport is certainly 3D, and its temperature dependence is of special interest. We have measured several crystals and present below examples of typical behavior.

Figure 3 shows the ρ_c data for two crystals annealed in air at 800 °C: $c1$ and $c2$, each in two states, quenched (curves $c1_q$ and $c2_q$) and aged ($c1_a$ and $c2_a$). They certainly do not follow log T, but perfectly fit the $T^{1/3}$ representation (1) with α of different signs; see inset. Hence, these aged and quenched states should be placed on different sides of the metal–insulator transition. All the data presented were obtained with a magnetic field of 7.7 T, but the magnetoresistance was small and did not affect the representation.

In the left-hand part of Fig. 3 we present in addition the curve $c1'_q$ obtained for the crystal $c1$ annealed at 780 °C and quenched; the curve is fit by Eq. (4) with $\sigma_0 = 1.5\alpha = 0.18$ S/cm. The aged state of the crystal with this oxygen content reveals symptoms of superconductivity, such as the onset of a kink and positive magnetoresistance at lower temperatures. Hence, these aged and quenched states should be placed on

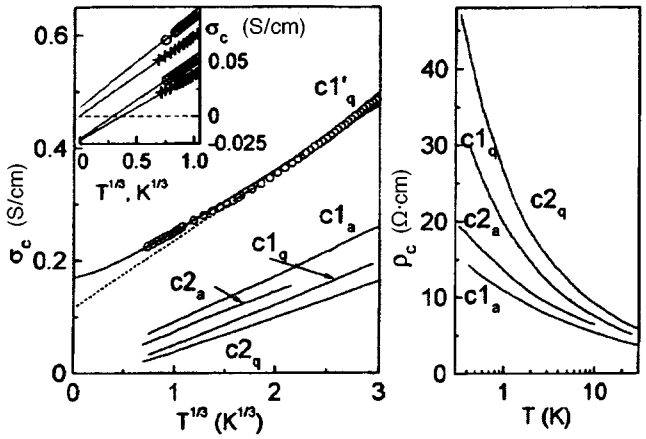

FIG. 3. Vertical resistivity data for two crystals, $c1$ and $c2$, plotted as σ_c versus $T^{1/3}$ (left) and as ρ_c versus $\log T$ (right). The experimental points have been removed from several of the curves. The inset shows an enlarged part of the main plot.

different sides of the superconductor–normal-metal transition on the phase diagram in Figs. 5 and 7 of Ref. 16. According to these diagrams, in the 800 °C range of annealing temperatures a 20° change results in a difference of $\Delta x \approx 0.025$ in the oxygen content and in a difference of $\Delta n/n_c \approx 0.07$ in the hole concentration n normalized to the critical value n_c. Although the precise positions of the two transitions may depend on the degree of disorder in the crystals, the numbers obtained can be regarded as estimates of the distance between the superconductor–normal-metal and the metal–insulator transitions along the abscissa of the phase diagram.

In conclusion, the low-temperature $\rho_c(T)$ curves of $YBa_2Cu_3O_{6+x}$ ($x \approx 0.37$) single crystals follow a scaling temperature dependence in the vicinity of the metal–insulator transition and permit one to specify the transition point. The difference in the oxygen concentration x between this point and that of the normal-metal–superconductor transition is approximately $\Delta x \approx 0.025$. It remains still unclear whether the representation of the in-plane resistivity $\rho_{ab}(T)$ in the region between these transitions on a log T scale is meaningful or whether the description by the functions (1) and (4) is more adequate.

The authors would like to thank A. Gerber, Y. Imry, and D. Khmel'nitskiĭ for helpful discussions. This work was supported by Grants RFFI 96-02-17497 and INTAS-RFBR 95-302 and by the Programs ''Superconductivity'' and ''Statistical Physics'' from the Russian Ministry of Science.

[a] e-mail: gantm@issp.ac.ru
[b] e-mail: lavrov@casper.che.nsk.su

[1] E. Abrahams, P. W. Anderson, D. C. Licciardello, and T. V. Ramakrishnan, Phys. Rev. Lett. **42**, 673 (1979).
[2] Y. Imry, J. Appl. Phys. **52**, 1817 (1981).
[3] B. L. Altshuler and A. G. Aronov, in *Electron–Electron Interactions in Disordered Systems*, A. L. Efros and M. Pollak, eds., Amsterdam: North-Holland, 1985.

[4] N. F. Mott, *Metal–Insulator Transitions*, 2nd ed., London: Taylor and Francis, 1990.
[5] B. I. Shklovskii and A. L. Efros, *Electronic Properties of Doped Semiconductors*, Berlin: Springer, 1984.
[6] V. F. Gantmakher, V. N. Zverev, V. M. Teplinskiĭ, and O. I. Barkalov, Zh. Éksp. Teor. **103**, 1460 (1993) [JETP **76**, 714 (1993)].
[7] D. B. Haviland, Y. Liu, and A. M. Goldman, Phys. Rev. Lett. **62**, 2180 (1989).
[8] G. Deutscher, B. Bandyopadhyay, T. Chui *et al.*, Phys. Rev. Lett. **44**, 1150 (1980).
[9] R. W. Simon, B. J. Dalrymple, D. van Vechten *et al.*, Phys. Rev. **36**, 1962 (1987).
[10] A. Gerber, J. Phys.: Condens. Matter **2**, 8167 (1990).
[11] V. Radhakrishnan, C. K. Subramaniam, V. Sankaranarayanan *et al.*, Physica C **167**, 53 (1990).
[12] Y. Ando, G. S. Boebinger, A. Passner *et al.*, Phys. Rev. Lett. **75**, 4662 (1995).
[13] Y. Ando, G. S. Boebinger, A. Passner *et al.*, J. Low Temp. Phys. **105**, 867 (1996).
[14] V. F. Gantmakher, V. V. Sinitsyn, G. E. Tsydynzhapov *et al.*, JETP Lett. **65,** 476 (1997).
[15] H. Claus, S. Yang, A. P. Paulicas, *et al.*, Physica C **171**, 205 (1990).
[16] A. N. Lavrov and L. P. Kozeeva, Physica C **253**, 313 (1995).
[17] A. N. Lavrov and L. P. Kozeeva, Physica C **248**, 365 (1995).
[18] B. W. Veal and A. P. Paulicas, Physica C **184**, 321 (1991).
[19] G. V. Uimin, V. F. Gantmakher, A. M. Neminsky *et al.*, Physica C **192**, 481 (1992).
[20] A. M. Neminsky and D. V. Shovkun, Physica C **252**, 327 (1995).
[21] D. A. Brawner, Z. Z. Wang, and N. P. Ong, Phys. Rev. B. **40**, 9329 (1989).

Published in English in the original Russian journal. Edited by Steve Torstveit.

Two-dimensional electron gas in double quantum wells with tilted bands

V. B. Timofeev, A. V. Larionov, P. S. Dorozhkin, M. Bayer, A. Forchel, and J. Straka

Institute of Solid-State Physics, Russian Academy of Sciences, 142432 Chernogolovka, Russia; Universität Würzburg, Technische Physik, Am Hubland, D-97074 Würzburg, Germany

(Submitted 15 May 1997)
Pis'ma Zh. Éksp. Teor. Fiz. **65**, No. 11, 840–845 (10 June 1997)

When a voltage is applied to double quantum wells based on AlGaAs/GaAs heterostructures with contact regions (**n**–**i**–**n** structures), a two-dimensional (2D) electron gas appears in one of the quantum wells. Under illumination which generates electron–hole pairs, the photoexcited holes become localized in a neighboring quantum well and recombine radiatively with the 2D electrons (tunneling recombination through the barrier). The appearance, ground-state energy, and density of the degenerate 2D electron gas are determined from the structure of the Landau levels in the luminescence and luminescence excitation spectra as well as from the oscillations of the radiative recombination intensity in a magnetic field with detection directly at the Fermi level. The electron density is regulated by the voltage between the contact regions and increases with the slope of the bands. For a fixed slope of the bands the 2D-electron density has an upper limit determined by the resonance tunneling of electrons into a neighboring quantum well and subsequent direct recombination with photoexcited holes. © *1997 American Institute of Physics.* [S0021-3640(97)00811-6]

PACS numbers: 73.20.Dx

1. Tunneling-coupled quantum systems, double quantum wells (DQWs) and superlattices, have long been a focus of interest in research on semiconductor heterostructures.[1–4] In the case of DQWs to which a band-tilting electrical bias is applied, this interest is due to the expected possibility of optical excitation of excitons in which the electron and hole occupy different wells separated by a barrier. Such excitons are called spatially indirect (interwell) in contrast to spatially direct (intrawell) excitons, in which the electron and hole occupy the same quantum well. Since interwell excitons should possess long lifetimes (long times for tunneling recombination through the barrier), they should not be difficult to store, and it seems that a gas of such excitons could be cooled to quite low temperatures. Theoretical works predict very interesting collective properties of such a gas of interacting excitons at critical densities and low temperatures.[6–9] The observation of unexpected collective properties in an interacting gas of such excitons has been reported.[5]

2. In this letter we demonstrate that events unfold according to a different scenario

in **n**–**i**–**n** AlGaAs/GaAs DQWs with tilted bands. It turns out that the nonequilibrium **e**–**h** pairs, spatially separated by a barrier on account of the band tilting, are mainly localized in the planes of the wells on fluctuations of the random potential if their density is less than the density of surface states ($n_c \sim 10^{10}$–10^{11} cm^{-2}) and the temperatures are sufficiently low. The luminescence in this case is determined mainly by the radiative recombination of randomly distributed **e**–**h** pairs which are localized in the planes and in which the electron and hole are separated by a barrier. If the density of nonequilibrium electrons (or holes) is higher than a certain critical density of localized states, which determines the mobility threshold, a two-dimensional gas will arise in the corresponding channel (quantum well). We shall show that a 2D-electron gas arises in such structures.

3. In the present work we investigated **n**–**i**–**n** AlGaAs/GaAs ($x=0.2$) DQWs grown by molecular-beam epitaxy on an **n**-GaAs (001) buffer substrate. The density of the **n**-type dopant (Si) in the substrate was equal to 3×10^{18} cm^{-3}. The GaAs quantum wells and the AlGaAs barrier between them were 100 and 45 Å wide, respectively. The DQWs were arranged symmetrically between AlGaAs insulating layers up to 3000 Å thick. Doped AlGaAs ($\mathbf{n}(\mathrm{Si})=3\times10^{18}$ cm^{-3}) layers with metallic conductivity were located directly behind the insulating layers. Thus the structures formed a capacitor with a DQW at the center. In the absence of voltage the structures exhibited properties corresponding to a flat-band regime. When a band-bending voltage was applied, current started to flow through the structure. The dark current density through the structure did not exceed 10 mA/cm^2 at the maximum voltages employed (± 3 V).

The samples were placed in a helium cryostat inside a superconducting solenoid. All experiments were conducted at a temperature of 2 K. An optical waveguide technique was used for photoexcitation and collection of the luminescence signal. Luminescence was excited with a Ne–He laser generating nonequilibrium **e**–**h** pairs in the quantum wells. The luminescence excitation spectra were measured with a Ti–sapphire laser, which in turn was excited by all lasing lines of an Ar laser. The luminescence signal was detected with a cooled photomultiplier and recorded in the photon-counting mode.

4. Figure 1 displays the luminescence spectra corresponding to radiative recombination of 2D electrons, which appear when a voltage is applied, in the bottom field-tilted quantum well with photoexcited holes in the neighboring quantum well (the optical transition scheme is shown in Fig. 2). Such recombination is of a tunneling nature and is determined by the overlapping of the wave functions of the 2D electrons and holes which ''leak'' under the barrier which spatially separates these carriers. Of course, on account of the inclination of the bands, the luminescence spectrum lies on the low-energy side of the term of the direct, symmetric, heavy-hole excitonic state (1sHH) in the neighboring quantum well where the electron density is low (see Fig. 2).

In zero magnetic field the luminescence spectrum is nearly square. This reflects the fact that the 2D-electron density of states is constant and the probability of radiative recombination is virtually independent of the wave vector.[10] The width of the spectrum corresponds to the Fermi energy of the 2D electrons. In a magnetic field oriented perpendicular to the layers, a structure associated with the Landau quantization of the electrons first appears in the spectrum for $B \geqslant 1.5$ T. From the magnitude of the splitting one easily obtains their cyclotron mass: $m_e \simeq 0.07 m_0$. The measured splittings in the luminescence spectrum with different values of B can also be used to construct a fan of Landau

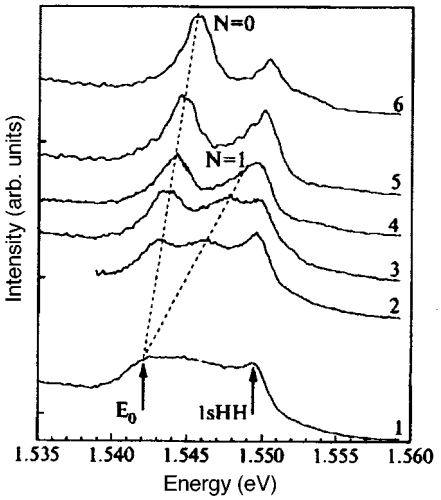

FIG. 1. Spectra of radiative recombination of 2D electrons with photoexcited holes from a neighboring quantum well as a function of the magnetic field. The numbers *1, 2, 3, 4, 5,* and *6* correspond to magnetic fields of 0, 1.5, 2, 2.5, 3, and 4 T, respectively. The applied voltage equals -2.5 V.

levels (see Fig. 3a, open dots). It is not difficult to determine from such a construction the energy E_0 of the 2D-electron band bottom (this energy corresponds to the lowest electronic size-quantization level in the lower electric-field-tilted quantum well) and the Fermi level E_F of the 2D electrons. The 2D-electron density found in this way is $n_s \simeq 2.2\times 10^{11}$ cm^{-2}. We emphasize that the luminescence spectra and their shape were found to be independent of the laser excitation power in the interval 10 μW–5 mW. This means that in the experimental optical-pumping interval the 2D-electron channel can be filled with electrons from the **n**-type contact region.

The electron density can be found in an independent optical experiment. For this, the intensity of the luminescence of 2D electrons directly at the Fermi level must be recorded as a function of the magnetic field. The oscillations of the intensity of the recombination radiation (which are shown by the solid curve in Fig. 3b) observed in such an experiment reflect the oscillations of the density of states at the Fermi level. The Fermi energy and the 2D-electron density are determined according to the period of these oscillations in terms of the reciprocal of the magnetic field. The observed oscillations of the luminescence intensity are essentially the optical analog of Shubnikov oscillations.[10]

The structure of the Landau levels of the 2D electrons is also observed in the luminescence excitation spectra. In the case at hand, we are talking about optical transitions to unfilled Landau levels lying immediately above the Fermi level. These spectra are displayed in Fig. 4, where, first of all, the lines of the ground states of excitons with heavy (1sHH) and light (1sLH) holes dominate. These excitonic lines correspond to direct transitions in excitonic states in a quantum well free of a 2D-electron gas. Together with the main excitonic lines, a new discrete line structure appears in the spectra measured in a magnetic field. As the magnetic field increases, these lines move rapidly to higher energies, in contrast with the lines of the excitonic ground states, which undergo

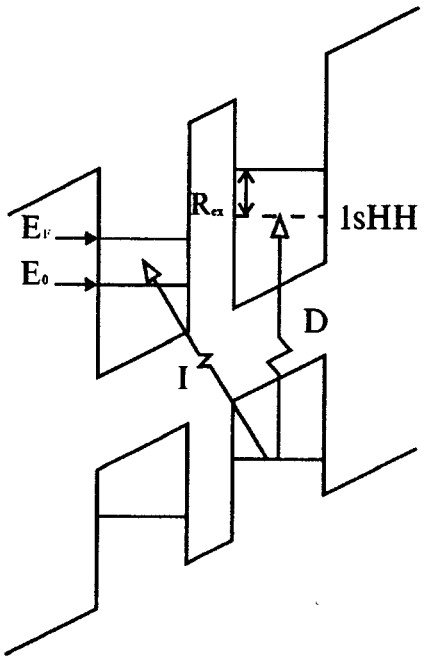

FIG. 2. Scheme of optical transitions in a AlGaAs/GaAs ($x=0.2$) DQW with an applied voltage. The arrows show the transition corresponding to the radiative recombination of 2D electrons with photoexcited holes from a neighboring quantum well (indirect transition) and transition corresponding to the term of a heavy-hole intrawell exciton — 1sHH (direct transition).

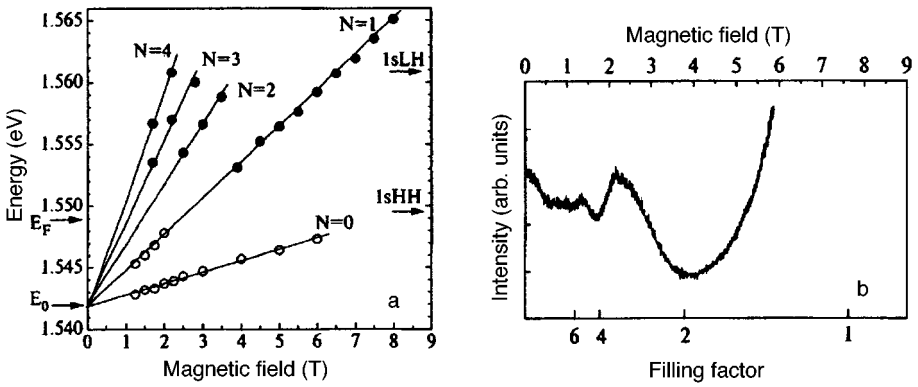

FIG. 3. a) Fan of Landau levels of 2D electrons. The open dots correspond to the luminescence and the filled dots to the excitation of luminescence of 2D electrons. The arrows show the positions of the Fermi levels and the 2D-electron band bottom and the positions of the terms of light-hole (1sLH) and heavy-hole (1sHH) intrawell excitons. The applied voltage equals -2.5 V. b) Intensity oscillations corresponding to radiative recombination of 2D electrons with photoexcited holes from the neighboring quantum well with detection directly at the Fermi level. The applied voltage equals -2.5 V.

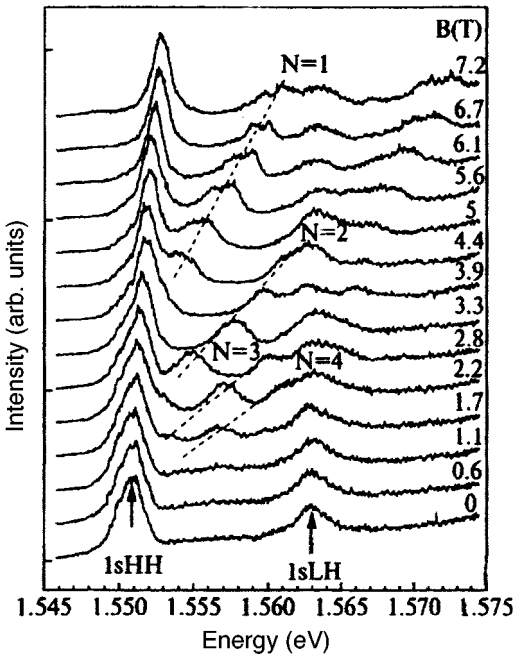

FIG. 4. Luminescence excitation spectra of 2D electrons as a function of the magnetic field. The arrows mark the positions of the terms of light-hole (1sLH) and heavy-hole (1sHH) intrawell excitons for $B=0$ T. The dashed straight lines correspond to optical transitions to unfilled Landau levels lying directly above the Fermi level. The applied external voltage equals -2.5 V.

a relatively small diamagnetic shift. The spectral positions of these lines measured with different magnetic fields are presented in Fig. 3a (filled dots). One can see that the energies of these lines fall, surprisingly accurately, on a fan of Landau levels. It is completely obvious that the discrete structure observed in the luminescence excitation spectra in a magnetic field corresponds to optical transitions of 2D electrons lying above the Fermi level to unfilled Landau levels. In the case at hand the optical transitions occur between hole states in one of the wells and the Landau levels of 2D electrons in another well. It follows from the conservation laws that an optical transition corresponds to **e**–**h** pair production in a quantum well with no 2D electrons followed by resonance tunneling of the photoexcited electron into a Landau level in a neighboring well. Why such transitions have such a large oscillator strength, comparable to that of a transition to the excitonic ground state, remains surprising.

The technique described above was used to study the behavior of a 2D-electron gas under different applied voltages. It was found that the Fermi level is always pinned by the spectral position of the 1sHH exciton in the neighboring well. This means that for a fixed voltage the 2D-electron density is limited from above by resonance tunneling of the electrons into the neighboring well, binding with photoexcited holes into an intrawell 1sHH exciton, and subsequent radiative annihilation of these excitons. The 2D-electron density can be varied by applying a voltage that regulates the slope of the electronic

bands and thereby changes the position E_0 of the 2D-electron band bottom. It was established that the free 2D-electron gas vanishes at voltages $V_g \simeq 0.7$ V. From this we estimated the critical density of surface electron states, which correspond to the mobility threshold or the metal–insulator transition in the 2D channel, obtaining a value $n_0 \simeq 5 \times 10^{10}$ cm^{-2}. At such and lower densities of nonequilibrium **e**–**h** excitations, radiative recombination of randomly distributed electron–hole pairs which are localized in the planes and in which the electron and hole are spatially separated by a barrier is manifested in the luminescence spectra. However, this requires a separate discussion and will be the subject of a separate publication.

We thank I. V. Kukushkin for interesting discussions of the questions touched upon in this letter. We thank the Russian Fund for Fundamental Research (Grant 96-02-17535), the Scientific-Technical Program ''Physics of Solid-State Nanostructures,'' and INTAS (Grant No. 576i-95) for supporting these investigations.

[1] Y. J. Chen, E. S. Koteles, B. S. Elman, and C. A. Arimento, Phys. Rev. B **36**, 4562 (1987).
[2] M. N. Islam, R. L. Hillman, D. A. Miller *et al.*, Appl. Phys. Lett. **50**, 1098 (1987).
[3] J. E. Golub, K. Kash, J. P. Harbison, and L. T. Florez, Phys. Rev. B **41**, 8564 (1990).
[4] T. Fukuzawa, E. E. Mendez, and J. M. Wang, Phys. Rev. Lett. **64**, 3066 (1990).
[5] L. V. Butov, A. Zrenner, G. Abstreiter *et al.*, Phys. Rev. Lett. **73**, 304 (1994).
[6] Yu. E. Lozovik and V. Yudson, Zh. Éksp. Teor. Fiz. **71**, 738 (1976) [Sov. Phys. JETP **44**, 389 (1976)].
[7] I. V. Lerner and Yu. E. Lozovik, Zh. Éksp. Teor. Fiz. **78**, 1167 (1980) [Sov. Phys. JETP **51**, 588 (1980)].
[8] D. Yoshioka and MacDonald, J. Phys. Soc. Jpn. **59**, 4211 (1990).
[9] X. M. Chen and J. J. Quinn, Phys. Rev. Lett. **67**, 895 (1991).
[10] I. V. Kukushkin and V. B. Timofeev, Adv. Phys. **45**, 147–242 (1996).

Translated by M. E. Alferieff

Determination of the parameters of photoinduced centers in glassy $GeS_{2.2}$ from the noise spectrum of the optical electroabsorption signal

É. N. Voronkov
Moscow Power Engineering Institute, 111250 Moscow, Russia

S. A. Kozyukhin and S. A. Khirin
N. S. Kurnakov Institute of General Inorganic Chemistry, Russian Academy of Sciences, 117509 Moscow, Russia

(Submitted 18 April 1997)
Pis'ma Zh. Éksp. Teor. Fiz. **65**, No. 11, 846–850 (10 June 1997)

It is found that the onset of photoinduced centers in glassy $GeS_{2.2}$ leads to chaotic changes in the signal in the long-wavelength region of the electroabsorption spectrum. It is shown that the application of noise spectroscopy methods to the analysis of the photoinduced signal makes it possible to determine the energy position of four levels of photoinduced centers, lying near the center of the band gap. The model of electron–hole pairs localized on defects is used to explain the position of the levels. © *1997 American Institute of Physics.* [S0021-3640(97)00911-0]

PACS numbers: 71.23.Cq, 78.66.Jg, 42.65.Sf

In glassy chalcogenide semiconductors (GCSs), energy transfer from a photoexcited electronic subsystem of the disordered matrix is accompanied by the appearance of photoinduced states, whose interaction results in photostructural transformations and could be responsible for photoinduced anisotropy,[1] optical instability,[2] the formation of metastable clusters, and light-induced phase transitions.[3,4] A great deal of attention is now being devoted to the investigation of these effects. From the standpoint of applications, this is explained by that fact that GCSs show promise as media for reversible writing of optical information. They can also be used in the fabrication of efficient optical waveguides, and experimental results on the control of light by light are now available. At the same time, the investigation of photostructural transformations in GCSs will enable advances in the solution of a number of fundamental questions in the physics of disordered materials, concerning the clarification of the mechanisms of structural self-ordering under external influences.

The present work was motivated by the desire to explain the experimental data obtained in Ref. 5, where it was shown that under intense illumination the optical electroabsorption spectrum of GeS_2 becomes unstable at long wavelengths and it was conjectured that the change in the electroabsorption signal reflects the dynamics of photostructural transformations. Since the photoinduced signal oscillates chaotically in time, it can be regarded as a noise caused by the appearance and decay of photoinduced defects. Accordingly, our objective in the present work was to determine, using the methods of

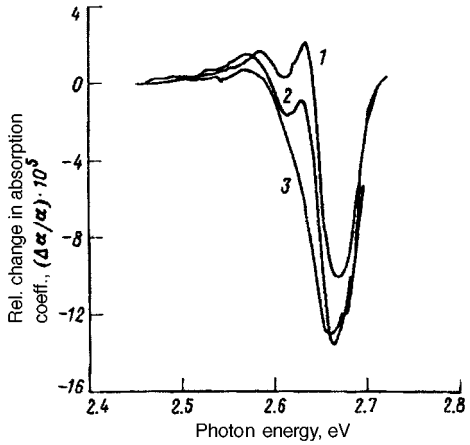

FIG. 1. Curves of electroabsorption in $GeS_{2.2}$ measured at successive times (*1* — initially, *2* — after 50 min, *3* — after 100 min).

noise spectroscopy of semiconductors, the parameters of the energy levels participating in the formation of defects.

We chose as the experimental material $GeS_{2.2}$, since optical bistability has been observed in GeS_2 (Ref. 3) and attributed[4] to the formation of a superstructure. The higher sulfur content in our experimental material was motivated by a desire to shift the fundamental absorption edge to longer wavelengths. The measurement procedure is described in detail in Ref. 5.

The electroabsorption signal is displayed in Figure 1. Curve *1* corresponds to measurements performed without intense external illumination (the spectrum is stable and highly reproducible), and curves *2* and *3* were measured 30 and 40 min, respectively, after the illumination was turned on. As one can see from the figure, the spectra become unstable after the illumination is turned on.

The relative temporal variation of the electroabsorption signal at a wavelength of 472 nm is shown in Fig. 2. The temporal variations of the signal at other wavelengths were similar: several slow oscillations followed by chaotic oscillations around a slowly varying value. When the exciting light is turned off, the light-induced signal gradually decays and a stationary electroabsorption spectrum is established. Oscillations similar to those shown in Fig. 2 have been observed[2] in the optical absorption by GCSs but their frequency was approximately an order of magnitude higher, which is attributable to the high laser illumination intensity in Ref. 2 and the heating of the sample. No parameters of the photoinduced centers have been determined, either in Ref. 2 or in later works, from the chaotically varying optical absorption signal.

The following conclusions can be drawn on the basis of the data presented in Figs. 1 and 2: The observed changes in the electroabsorption signal characterize the change in the occupancy[6] of levels lying in the tails of states in the mobility gap (the gap width for the experimental material equals approximately 2.7 eV). Since under intense external

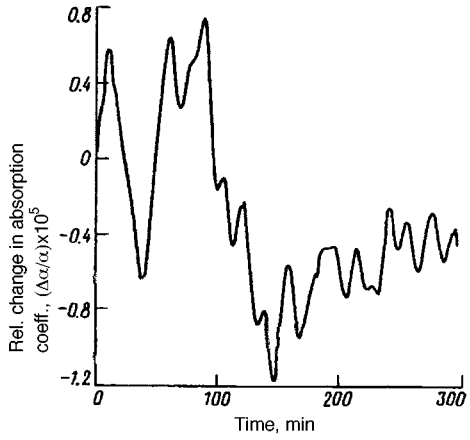

FIG. 2. Temporal fluctuations of the electroabsorption signal.

illumination the Fermi quasilevels lie near the edges of the mobility gap, the observed change in the signal reflects the kinetics of the variation of the occupancy of the levels participating in the optical transitions. The level occupancy in turn is controlled by trapping on deep recombination centers. Therefore the change in occupancy is due to the formation of photoinduced recombination centers, since the processes by which charge carriers escape from shallow electronic levels lying in the tails of the states and then recombine are several orders of magnitude faster than is observed experimentally.

To investigate the character of the random fluctuations of the electrooptic signal, a Fourier analysis of the dependence shown in Fig. 2 was performed. The corresponding frequency spectrum is displayed in Fig. 3. This spectrum is described well by a superposition of several terms of the form $A_i/(1+\omega^2\tau_i^2)$. This attests to the presence of several centers characterized by different time constants. It should be noted that the investigation of the kinetics of photoinduced effects showed that the relaxation of photoinduced absorption and photoinduced anisotropy can be approximated in a wide time interval by a ''fractional'' exponential function $\exp(-t/\tau)^\gamma$ where the exponent lies in the

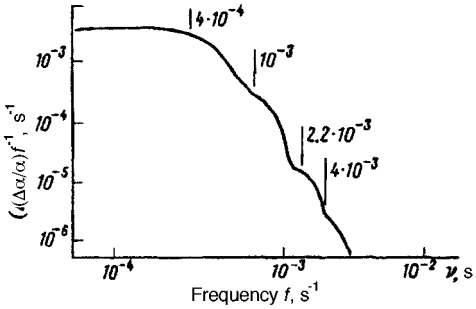

FIG. 3. Frequency spectrum of the fluctuations of the electroabsorption signal.

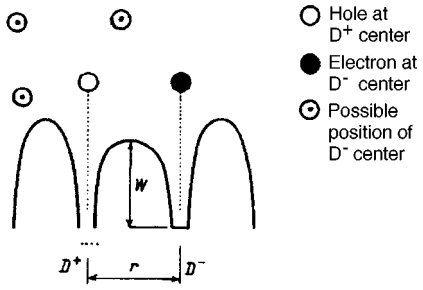

FIG. 4. Arrangement of a photoinduced center.

range $0<\gamma<1$ and the time constant τ is determined by the recording time (Kohlrausch's law). In Ref. 1 relaxation of this kind is attributed to the hierarchical nature of the bounds on its dynamics, i.e., the existence of a hierarchy of structural elements and, accordingly, processes with different characteristic times.

To explain the results obtained we proceeded from the Mott–Street model,[6,7] according to which two types of defects D^+ and D^- (a variable-valence pair) can form in chalcogenide materials and the strong electron–phonon interaction accompanying the trapping of an electron on a defect and the appearance of a D^- center shift the energy level of the defect from the conduction band edge toward the valence band. Such centers could be responsible for the pinning of the Fermi level near the center of the mobility gap in glassy chalcogenide semiconductors. Street has proposed that the interaction of D^+ and D^- centers leads to vanishing of the trapped electron and hole and to a local modification of the structure.[7] The structural modification could be due to a displacement of a chalcogen atom, whose position is determined by one of the minima on the double-well configuration–coordinate diagram.[8]

The recombination of an electron and a hole localized close to one another can be regarded as a ''pair'' recombination process, which is characteristic for low-mobility materials. The essence of the effect is that the electron and hole do not have enough time to separate over the thermalization time to a distance at which the Coulomb interaction is eliminated. In a material with a disordered structure and a high defect density it is very likely that during the thermalization of an electron–hole pair the electron and hole will be trapped before they separate to a distance at which the interaction between them vanishes. Therefore the electron and hole are located in a potential well which is formed by the Coulomb interaction. In consequence, sooner or later they will recombine, since the probability of such recombination is much higher than the probability of the electron and hole being separately transferred into widely separated states.

It is conjectured that light induces the formation of D^+–D^- pairs with an electron and hole localized close to each other on defects. A barrier whose height depends on the relative arrangement of the charged defects impedes recombination.

The corresponding scheme is displayed in Fig. 4.

A transition of an electron from a D^- center to a D^+ center in a neighboring well

followed by recombination of the electron can occur by a hopping mechanism. The hopping frequency can be written as

$$\nu = \nu_{\text{ph}} \exp(-2\alpha r - W/kT), \tag{1}$$

where ν_{ph} is the phonon frequency, α is a localization parameter, $W = W_0 - U(r)$ is the height of the barrier between the D^+ and D^- centers, W_0 is the energy corresponding to the excitation of an electron at the edge of the mobility gap for a isolated D^- center, and R is the distance between the D^+ and D^- centers.

The Coulomb interaction energy is

$$U(r) = q^2/4\pi\epsilon\epsilon_0 r. \tag{2}$$

For the case of strong localization $\alpha r \ll W/kT$. We calculate the barrier heights W from Eq. (1) (ϵ was set equal to 5 in the calculations), taking $\nu_{\text{ph}} = 5 \times 10^{11}$ s^{-1} and using the experimentally determined frequencies (Fig. 3). The energy levels turn out to be very close to one another: 0.839, 0.857, 0.875, and 0.899 eV. The increase in the barrier height and the corresponding increase in the characteristic time are explained in the present model by an increase in the distance between the centers and a corresponding decrease in the Coulomb interaction.

The distance between the D^+ and D^- centers is important for further estimates. For the fastest center we take the minimum possible value, equal to the distance between neighboring chalcogen atoms: 3.8 Å. Then the Coulomb-induced decrease of the recombination-barrier height accompanying a change in the distance between the localized electron and hole can be estimated from expression (2). Thus the distance between the D^+ and D^- centers participating in the process can be estimated using the experimental values of the energies. The results are 3.80, 3.89, 3.98, and 4.12 Å.

An estimate of the barrier W_0 for an isolated D^- center gives 1.57 eV, which is somewhat greater than one-half the width of the mobility gap in $GeS_{2.2}$. These centers are not recorded in photostructural transformations under ordinary conditions because the corresponding time constant is very high and carriers are more likely to be ejected from a well. However, they can operate as efficient recombination centers and participate in the generation of D^+–D^- pairs; this process will be more intense under optical excitation conditions. As the D^+ and D^- pairs arise and the distance between the heteropolar centers decreases, the barrier between them will decrease and the probability of recombination of a localized pair and, accordingly, of a structural modification of the center will increase.

Several conclusions can be drawn from the foregoing analysis and the estimates made above.

The application of noise spectroscopy to the analysis of nonstationary electroabsorption spectra makes it possible to determine the parameters of the photoinduced centers in $GeS_{2.2}$, which are seen as deep recombination centers.

The hopping recombination mechanism makes it possible to explain the presence of centers with a very small splitting between the separate levels near the center of the band gap. The energy width of the band of these levels, which are manifested in photostructural transformations of $GeS_{2.2}$, can reach 0.7 eV.

A set of levels leads to a set of discrete times characterizing photostructural transformations in which D^+–D^- centers participate.

The nearest-neighbor environment of D^- is not symmetric and, accordingly, local anisotropic structures can form when D^+–D^- pairs vanish.

The Coulomb interaction of D^+–D^- centers can lead to the formation of local superstructures and superclusters with sizes of up to several tens of angstroms. Their sizes and density will depend on the density of D^+–D^- centers and, accordingly, on the illumination intensity.

The giant structures of the order of 1000 Å in size which were observed in Ref. 3 can arise if the density of D^+–D^- centers reaches 10^{18} cm^{-3}.

Unfortunately, the results of the present work do not permit making any conjectures about the physicochemical nature of the centers. It is very likely that dangling bonds are responsible for their appearance, but other explanations are also possible.[8]

It should also be noted that we have shown on the basis of this model that interacting defects should carry a heteropolar charge which vanishes on recombination. The energy released in the process gives rise to local overheating and structural modification of the center.

This work was supported by the Russian Fund for Fundamental Research under Project No. 96-02-19317.

We thank S. A. Dembovskiĭ for helpful discussions.

[1] V. K. Tikhomirov, JETP Lett. **57**, 821 (1993).
[2] J. Haito, G. Zantai, and J. Kosa Samogyi, Solid State Commun. **23**, 401 (1977).
[3] V. M. Lyubin and V. K. Tikhomirov, JETP Lett. **55**, 23 (1992).
[4] S. A. Dembovsky and P. A. Koz'min, Solid State Commun. **86**, 623 (1992).
[5] E. N. Voronkov, S. A. Kozukhin, and V. N. Hirin, Solid State Commun. **90**, 807 (1994).
[6] N. F. Mott and E. A. Davis, *Electron Processes in Non-Crystalline Materials*, Clarendon Press, Oxford, 1979.
[7] R. A. Street, Solid State Commun. **24**, 363 (1977).
[8] M. I. Klinger and V. G. Karpov, Zh. Éksp. Teor. Fiz. **82**, 1687 (1982) [Sov. Phys. JETP **55**, 976 (1982)].

Translated by M. E. Alferieff

On a classical analog of the isospectral Schrödinger problem

V. M. Eleonskiĭ,[a] V. G. Korolev,[b] and N. E. Kulagin
F. V. Lukin Scientific-Research Institute of Physical Problems State Science Center, 103460 Zelenograd, Moscow, Russia

(Submitted 14 April 1997; resubmitted 5 May 1997)
Pis'ma Zh. Éksp. Teor. Fiz. **65**, No. 11, 851–854 (10 June 1997)

It is shown that the problem of potential deformations that preserve the energy dependence of the oscillation frequency corresponds in the classical limit to the isospectral problem for the Schrödinger equation. The solutions of the corresponding evolutionary equations for the potential (with respect to the deformation parameter) are simple Riemann waves. The relation between such solutions and the solutions of the inverse problem of mechanics — the problem of reconstructing the potential given the energy dependence of the oscillation frequency — is determined. © *1997 American Institute of Physics.*
[S0021-3640(97)01011-6]

PACS numbers: 03.65.Ge, 03.20.+i, 03.40.Kf

The problem of isospectral deformations, which are determined by the corresponding phase flows,[1,2] of the potential in the Schrödinger equation can be associated to a definite class of evolutionary (with respect to the deformation parameter) equations for the characteristic elements of the Schrödinger problem and the potential.[3] The following equations correspond to the isospectral problem in the simplest case of a point spectrum:

$$-\frac{\hbar^2}{2\mu}(\psi_E)_{xx}+U(x,\tau)\psi_E=E\psi_E, \qquad \lim_{x\to\pm\infty}\psi_E=0; \tag{1}$$

$$E_\tau=0, \quad \frac{\hbar^2}{2\mu}\left[\frac{(\psi_E)_x}{\psi_E}\right]_\tau=\frac{1}{2}\alpha(\tau)\psi_E^2, \quad U_\tau=\alpha(\psi_E^2)_x, \tag{2}$$

where τ is the deformation parameter. The last relation in Eq. (2) determines the simplest (individual) phase flow induced by a selected characteristic element of the Schrödinger problem (1); $\alpha(\tau)>0$ is an arbitrary function of τ. As shown in Ref. 3, the equation describing the isospectral deformation of the potential (and obtained from Eqs. (1) and (2)) for the particular case indicated can be put into the form of the well-known Liouville equation $S_{xt}=\exp S$, which is satisfied, specifically, by the family of potentials corresponding to an equidistant energy spectrum. In the classical limit $\hbar\to 0$, some members of this family degenerate into potentials for which the classical motion is isochronous (the period is energy-independent),[4] specifically, the harmonic-oscillator potential.

There arises in this connection the question: What is the classical limit (or analog) of the quantum-mechanical isospectral problem itself?

It is well known that in the classical limit ($\hbar \to 0$, $\psi \to \sqrt{\rho} e^{iS/\hbar}$) the Schrödinger equation leads to the Hamilton–Jacobi and continuity equations:[5,6]

$$E = \frac{1}{2\mu}(S_x)^2 + U(x,\tau), \quad (\rho S_x)_x = 0. \tag{3}$$

Following the logic of the quantum isospectral problem,[2,3] we supplement this pair of equations by an expression for the classical analog of the phase flow

$$U_\tau = \alpha(\tau)\rho_x. \tag{4}$$

At a fixed energy level $E = E_0$, such that $(E_0)_\tau = 0$, the equations (3) and (4) lead to the following evolutionary equation for the function $S(x,\tau,E_0)$:

$$\left[\frac{1}{2\mu}(S_x)^2\right]_\tau + \alpha(\tau)\beta(\tau)\left(\frac{1}{|S_x|}\right)_x = 0. \tag{5}$$

Here $\beta(\tau) > 0$ is an arbitrary function which arises when the continuity equation is integrated; the sign of the modulus in Eq. (5) arises from the condition $\rho(x,\tau) > 0$. Switching to the velocity field $V(x,\tau) = \mu^{-1} S_x$ and to a new deformation parameter $\tau \to \tau = \mu^{-2} \int d\tau \alpha(\tau)\beta(\tau)$ puts Eq. (5) into the form

$$V_\tau - |V|^{-3} V_x = 0, \tag{6}$$

after which, on the strength of Eqs. (3)–(5), the evolutionary equation for the potential becomes

$$U_\tau - \left(\frac{\mu/2}{E_0 - U}\right)^{3/2} U_x = 0. \tag{7}$$

The solution of this equation (in the implicit form) is a simple Riemann wave:[7]

$$U(x,\tau) = U_0\left[x + \left(\frac{\mu/2}{E_0 - U}\right)^{3/2}\tau\right], \quad U(x,\tau)\big|_{\tau=0} = U_0(x). \tag{8}$$

Here $U_0(x)$ is the undeformed potential.

We shall show that the solution (8) describes a deformation of a classical potential U such that the initial energy dependence of the period $T(E)$ of the oscillations is preserved for any τ. We introduce the function W_0 inverse to U_0: $y = U_0(x)$, $x = W_0(y)$. In the general case the function W_0 possesses several branches $W_0^{(k)}$, even for a uniquely defined potential U_0. From Eq. (8) we find that the function $x(U,\tau)$ for each branch is determined by the expression

$$x^{(k)}(U,\tau) = W_0^{(k)}(U) - \left(\frac{\mu/2}{E_0 - U}\right)^{3/2}\tau. \tag{9}$$

Let us examine two neighboring branches $x^{(k')}$ and $x^{(k'')}$ forming a local minimum of the potential. As is well known,[8] the function $T(E)$ for motion in such a well satisfies the equation

$$x^{(k')}(U,\tau) - x^{(k'')}(U,\tau) = \int_{U_{\min}}^{U} \frac{T(E)dE}{\sqrt{U-E}}. \tag{10}$$

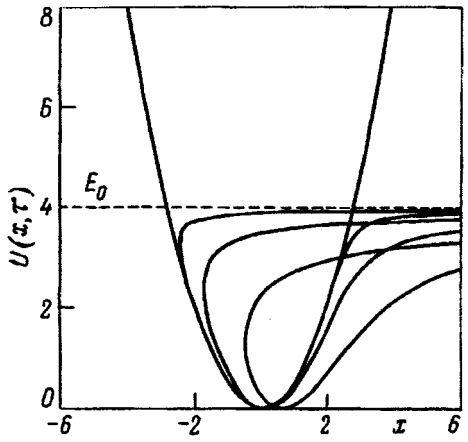

FIG. 1. Deformation of an isochronous potential in the one-flow case, $E_0=4$, $\tau=0$, 0.1, 1, 5.

By virtue of Eq. (9) the left-hand side of this relation does not depend on the deformation parameter τ. Therefore the function $T(E)$ for the potential $U(x,\tau)$ is the same as for $U_0(x)$ (we note that as the potential is deformed, the turning points $x^{(k)}=W_0^{(k)}\times(E)-[2(E_0-E)/\mu]^{-3/2}\tau$ move in a manner such that the distance between them remains unchanged).

Therefore the condition that the point spectrum of the energy eigenvalues of the quantum problem is independent of the deformation parameter of the potential corresponds in the classical problem to the condition that under a deformation the energy dependence of the oscillation frequency remains the same as in the case of the initial (undeformed) potential.[4]

Let us return to the solution (8). As a result of the evolution with respect to the deformation parameter, the potential, as a rule, loses (as is characteristic for simple Riemann waves) its single-valuedness. In the case of an individual flow (4), considered above, the multivaluedness of the deformed potential arises immediately (at $\tau=0+$), and the above-indicated properties of the oscillation frequency obtain for finite τ only for energy levels $E\leqslant E_{\rm crit}<E_0$ for which the potential $U(x,\tau,E_0)$ is a single-valued function of x (Fig. 1).

Switching to the evolutionary equations for the potential induced by a collection of phase flows

$$U_\tau=\sum_{j=1}^{N}\alpha_j(\tau)(\rho_j)_x \tag{11}$$

at the selected levels E_1^0, E_2^0, ..., E_N^0, the system of equations (3) written for the levels $E=E_j^0$, $1\leqslant j\leqslant N$ yields an equation for a more general class of simple waves:

$$U_\tau-\sum_{j=1}^{N}\frac{\gamma(\tau)}{(E_j^0-U)^{3/2}}U_x=0. \tag{12}$$

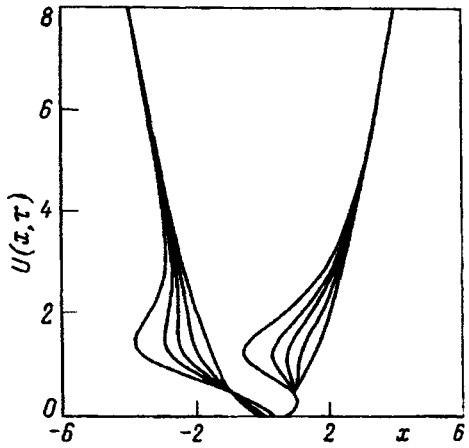

FIG. 2. Deformation of an isochronous potential in the two-flow case for $E_{1,2}=E_0\pm i\epsilon$, $E_0=\epsilon=1$; $\tau=0$, 0.5, 1.0, 1.5, and 2.5.

Let us examine the case of the deformation of the harmonic oscillator potential $U_0=(\omega x)^2/2$. In the case $N=2$ the solution of Eq. (12) has the form

$$x_\pm(U,\tau)=\pm\frac{\sqrt{2U}}{\omega}-\frac{\gamma_1\tau}{(E_1^0-U)^{3/2}}-\frac{\gamma_2\tau}{(E_2^0-U)^{3/2}},\quad \gamma_{1,2}=\text{const}. \tag{13}$$

Let $\gamma_1=\gamma_2=1/2$. To avoid singularities, let us displace the parameters E_1^0 and E_2^0 into the complex plane ($E_1^0\to E_0+i\epsilon$, $E_2^0\to E_0-i\epsilon$). As a result, we find that for values of the parameter τ such that $0\leqslant\tau<\tau_{\text{crit}}(E_0,\epsilon)$ and finite ϵ the deformed potential is isochronous for *all* $E<+\infty$. The critical value of τ is determined according to the well-known conditions for breaking of the simplest Riemann waves. A characteristic scenario of the deformation of the harmonic oscillator potential is displayed in Fig. 2.

In summary, enlarging the set of phase flows in Eq. (11) can delay the breaking of the potential in time. We note that in all cases the potential after the moment of breaking can always be determined, while preserving uniqueness, by the standard conditions employed in the analysis of the breaking of nonlinear waves.

In closing, we call attention to the fact that the evolutionary equations studied above for deformable potentials are related with the inverse problem of classical mechanics — the problem of reconstructing the potential from a prescribed energy dependence of the oscillation frequency. In the general case this problem is related[8] with the solution of equation (10). In the case of isochronous potentials ($T(E)=\text{const}(E)$) the solution of this problem is given by the relation

$$x_+(U)-x_-(U)=2\frac{\sqrt{2U}}{\omega}. \tag{14}$$

It is easy to show that this expression can also be written in the alternative form

$$U=\frac{1}{2}\omega^2[x-X(U)]^2. \tag{15}$$

Here $X(U)$ is an arbitrary function. Suppose that X depends on a parameter τ: $X=X(U,\tau)$. Differentiating expression (15) with respect to x and τ, we verify that $U(x,\tau)$ satisfies the equation

$$U_\tau+X_\tau(U,\tau)U_x=0. \tag{16}$$

The evolutionary equations for deformable potentials (12) engendered by the set of flows (11) can be identified with Eq. (16). Therefore the classical analog of the quantum isospectral problem is related with the inverse problem of classical mechanics.

[a)]e-mail: eleon@nonlin.msk.ru
[b)]e-mail: korolev@nonlin.msk.ru

[1]E. A. Kuznetsov and S. E. Fal'kovich, Phys. Lett. A **86**, 203 (1981).
[2]H. P. McKean and E. Trubowitz, Commun. Math. Phys. **82**, 471 (1982).
[3]V. M. Eleonsky and V. G. Korolev, Phys. Rev. A **55**, 2580 (1997).
[4]V. M. Eleonsky and V. G. Korolev, J. Phys. A **28**, 4973 (1995).
[5]V. A. Fok, *The Beginning of Quantum Mechanics* [in Russian], Nauka, Moscow, 1976.
[6]D. I. Blokhintsev, *The Philosophy of Quantum Mechanics*, D. Reidel, Dordrecht, Holland, 1968 [Russian original, Nauka, Moscow, 1987].
[7]G. B. Whitham, *Linear and Nonlinear Waves*, John Wiley, New York, 1974 [Russian translation, Mir, Moscow, 1977].
[8]L. D. Landau and E. M. Lifshitz, *Mechanics*, Pergamon Press, New York [Russian original, Nauka, Moscow, 1988].

Translated by M. E. Alferieff